

The haze and methane distributions on Neptune from HST–STIS spectroscopy

Erich Karkoschka*, Martin G. Tomasko

Lunar and Planetary Laboratory, University of Arizona, Tucson, AZ 85721-0092, United States

ARTICLE INFO

Article history:

Received 16 February 2010

Revised 19 August 2010

Accepted 19 August 2010

Available online 25 August 2010

Keywords:

Atmospheres, Composition

Atmospheres, Structure

Neptune

Neptune, Atmosphere

Spectroscopy

ABSTRACT

We analyzed a data cube of Neptune acquired with the Hubble STIS spectrograph on August 3, 2003. The data covered the full afternoon hemisphere at 0.1 arcsec spatial resolution between 300 and 1000 nm wavelength at 1 nm resolution. Navigation was accurate to 0.004 arcsec and 0.05 nm. We constrained the vertical aerosol structure with radiative transfer calculations. Ultraviolet data confirmed the presence of a stratospheric haze of optical depth 0.04 at 370 nm wavelength. Bright, discrete clouds, most abundant near latitudes -40° and 30° , had their top near the tropopause. They covered 1.7% of the observed disk if they were optically thick. The methane abundance above the cloud tops was 0.0026 and 0.0017 km-am for southern and northern clouds, respectively, identical to earlier observations by Sromovsky et al. (Sromovsky, L.A., Fry, P.M., Dowling, T.E., Baines, K.H., Limaye, S.S., [2001b]. *Icarus* 149, 459–488). Aside from these clouds, the upper troposphere was essentially clear. Below the 1.4-bar layer, a vertically uniform haze extended at least down to 10 bars with optical depth of 0.10–0.16/bar, depending on the latitude. Haze particles were bright at wavelengths above 600 nm, but darkened toward the ultraviolet, at the equator more so than at mid and high latitudes. A dark band near -60° latitude was caused by a 0.01 decrease of the single scattering albedo in the visible, which was close to unity. A comparison of methane and hydrogen absorptions contradicted the current view that methane is uniformly mixed in latitude and altitude below the ~ 1.5 -bar layer. The 0.04 ± 0.01 methane mixing ratio is only uniform at low latitudes. At high southern latitudes, it is depressed roughly between the 1.2 and 3.3-bar layers compared to low-latitude values. The maximum depression factor is ~ 2.7 at 1.8 bars. We present models with 2° latitude sampling across the full sunlit globe that fit the observed reflectivities to 2.8% rms.

© 2010 Elsevier Inc. All rights reserved.

1. Introduction

Neptune is probably the planet with the least accurate knowledge about the vertical haze and methane structure, which determines where most sunlight is deposited as heat or scattered back to the observer. Based on estimated condensation levels for methane and H_2S near 2 and 4 bars pressure, radiative transfer models with haze or clouds at both layers could explain several observations (Hammel et al., 1989; Baines and Smith, 1990; Baines and Hammel, 1994; Baines et al., 1995; Sromovsky et al., 2001b). The opacity just above the 2-bar layer was called methane haze considering an optical depth on the order of 0.1. The opacity at 3–4 bars was called the H_2S cloud since it was considered to be optically thick. Because of intrinsic difficulties of constraining the vertical haze and cloud structure, the altitudes of both layers were assumed and their optical depths were fitted to explain the observations.

Part of Neptune is covered by discrete clouds with a strong temporal variability (cf. references in Hammel and Lockwood (2007)).

Even the simplest models can easily place them within about a scale height of the tropopause (0.13 bars pressure).

Since almost all observations that constrain the haze and cloud structure involve methane absorptions, Neptune's structure was determined by assuming a reasonable vertical methane mixing ratio profile and then interpreting observed features as haze or cloud features. Whether these features could be caused by spatial variations of the methane mixing ratio has not been investigated. Recent mid-infrared images by Orton et al. (2007) indicate major horizontal variability of methane near the tropopause.

This is similar to our state of knowledge about the atmosphere of Uranus several years ago. However, recent work on Uranus revealed that there is no significant observable aerosol enhancement at the methane condensation level (Sromovsky and Fry, 2007), nor at the H_2S condensation level (Karkoschka and Tomasko, 2009). The latter work, which we call K&T2009, explained the main observed feature primarily as a latitudinal methane feature and not a haze feature. This investigation was based on a data cube of Uranus, providing images at the spatial resolution of the Hubble Space Telescope (HST) in 1750 wavelengths.

We acquired a similar data cube of Neptune, and we present here its calibration, analysis, and modeling using the methods of

* Corresponding author. Fax: +1 520 621 4933.

E-mail address: erich@lpl.arizona.edu (E. Karkoschka).

K&T2009. We do not repeat the methods here, but focus on additional techniques needed because of the characteristics of the Neptune data. In order to give a rough idea about the pressure levels probed by our Neptune data, we show cumulative optical depths for Rayleigh scattering, methane and hydrogen absorption, and aerosol extinction in Fig. 1.

Our observations occurred on August 3, 2003, just before Neptune's northern winter solstice. Within the 50+ year long photometric record of Neptune in blue and green filters, our observations were taken after Neptune had brightened for some 20 years with some indication of leveling off during the years after our observations (Hammel and Lockwood, 2007).

The next section describes the observations and data calibration. Section 3 discusses discrete clouds, while the other features are discussed in Sections 4–7. Section 4 reports observed latitudinal variations. Section 5 explains our radiative transfer modeling technique. Section 6 discusses the distribution of tropospheric hazes and methane. Section 7 focuses on the comparison between Uranus and Neptune. Section 8 summarizes our work.

2. Data calibration

Our program GO 9330 consisted of 49 exposures taken with the Space Telescope Imaging Spectrograph (STIS). The four-orbit program was executed during seven successive, shortened HST orbits. The first two exposures were acquisition images in 530–1000 nm (F28X52LP) and clear filters (50CCD). Following were 28 exposures with the grating G750L covering the wavelengths 530–1020 nm at 0.49 nm/pixel. The slit was 0.1 arcsec wide and parallel to the central meridian of Neptune, stepping from the evening limb to the central meridian in 0.05 arcsec intervals. Along the slit, 140 samples were taken, of which Neptune took up to 47 pixels at 0.05 arcsec/pixel. One lamp exposure for wavelength calibration and five flatfields were also taken. The remaining 13 exposures used the grating G430L covering the wavelengths 290–570 nm at 0.27 nm/pixel, positioning the slit in 0.10 arcsec intervals from the evening limb to the central meridian. The observational parameters are summarized in Table 1.

The standard pipeline processing by the Space Telescope Science Institute (STScI) provided bias subtraction and standard flatfielding. We used the method of K&T2009 to restore 50,388 bad-pixel values (0.8% of all data) by interpolation from good pixels. The correction of flatfields for the variable slit width and for the CCD fringing was applied (cf. K&T2009), as was the correction for charge transfer efficiency of the CCD and for light scattered in the CCD.

Using the spectral calibration method of K&T2009, our spectral calibration had a random errors of 0.04 pixels rms (root mean square), corresponding to 0.01 nm (G430L) and 0.02 nm (G750L). We estimated the spectral calibration to be accurate to 0.05 nm.

We reduced the spectral data of 1750 wavelengths to the same 70 spectral bands of continuum and methane bands as in K&T2009. We replaced the 10 spectral bands near the 826 nm hydrogen absorption into five wider spectral bands in order to reduce noise, yielding a total of 75 spectral bands. Each of the five new bands consists of the average of two regions below and above 826 nm. Their relative weighting was selected to give all five bands the same geometric albedo of Neptune so that all five bands probe to the same amount of absorption in the atmosphere. This way, a significant variation of the latitudinal structure between the five bands implies a latitudinal variation of the methane mixing ratio. Appendix A gives examples for the definition of a few spectral bands.

Using the spatial calibration method of K&T2009, the individual navigation measurements differed by 0.04 pixels rms from our adopted smooth functions of time. We estimated the accuracy of spatial navigation at 0.08 pixels, corresponding to 0.004 arcsec. Our navigation indicated that for both spectral ranges, the first observation was just off the evening limb, and the last observation was just past the central meridian. Thus, the data covered the complete afternoon hemisphere. We resampled all data in steps of 0.025 equatorial radii of Neptune (0.029 arcsec), somewhat finer than the pixel size of the CCD (0.050 arcsec).

The deconvolution of the point spread function (PSF) of HST, albedo calibration, and correction for Raman scattering was done the same way as in K&T2009, but no correction was needed for Nep-

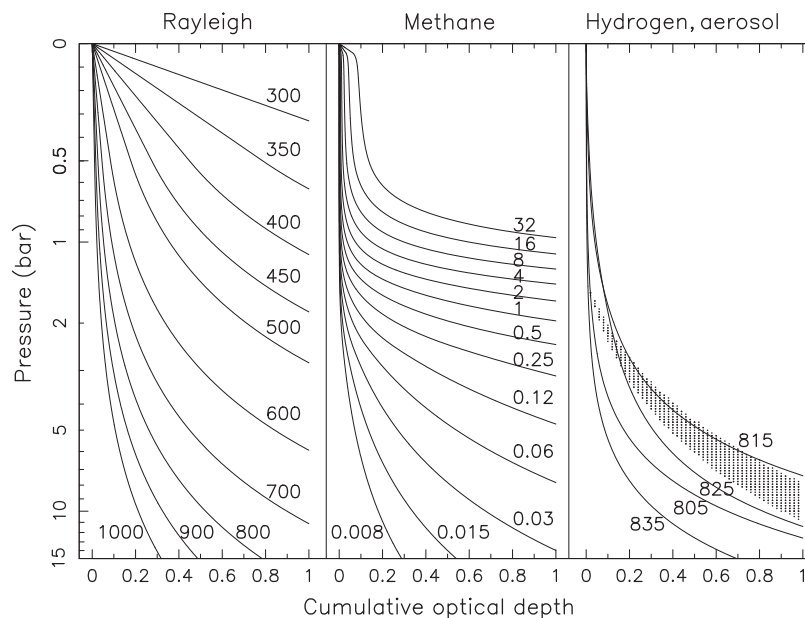


Fig. 1. The cumulative optical depth for Rayleigh scattering (left), methane absorption (middle), and hydrogen absorption (right) as function of pressure for the global average. In the left and right panels, wavelengths are labeled in nm. In the center panel, methane absorption coefficients are labeled in $\text{km}\cdot\text{am}^{-1}$. The right panel also displays the haze optical depth (shaded). Note that the pressure scale changes from linear to logarithmic at 0.5 bars.

Table 1
Observations.

Date	2003 August 3, 4:38–14:15 UT
Radius of Neptune	1.17 arcsec
Line of sight	28.2° below equator of Neptune
Phase angle	0.04°
Program ID	GO 9330
Instrument	HST–STIS
Gratings	G430L (290–570 nm), G750L (530–1020 nm)
Dispersion	0.27 nm/pixel (G430L) and 0.49 nm/pixel (G750L)
Spectral resolution	1 nm
Slit width	0.1 arcsec
Pixel size	0.05 arcsec (north–south on Neptune)
East–west sampling for G430L	13 exposures spaced 0.10 arcsec
East–west sampling for G750L	28 exposures spaced 0.05 arcsec
Spatial coverage	Complete afternoon hemisphere
Exposure time	160 s (G430L), 195 s (G750L) per Neptune exposure
Exposure level	400 electrons per data point (median)

tune’s rings. Raman scattering features on Neptune were about 10% stronger than on Uranus, and Neptune’s corrected spectra in the ultraviolet were almost as smooth as Uranus’. Similar to the conclusion for Uranus, we do not expect the Raman correction limiting the accuracy of our results, except maybe for the very weakest methane absorptions probing the deepest atmospheric levels. Our absolute reflectivity calibration is accurate to 5%. Relative reflectivities between different latitudes or nearby wavelengths or between Uranus and Neptune are accurate to about 1%. Our calibrated images are shown in Fig. 2.

3. Discrete clouds

3.1. Data analysis

The most obvious features on Neptune are discrete features, which we call discrete clouds. We analyzed discrete clouds based on the five images with at least 4 km-am^{−1} methane absorption coefficient, displayed in panel D of Fig. 2 (1 km-am = 2.687 × 10²⁴ molecules cm^{−2}). Although the same pattern of discrete clouds dominates images in weaker absorptions, detailed analysis indicates a subtle change of pattern for absorptions weaker than 4 km-am^{−1}, most likely caused by other features at lower altitudes.

We first analyzed the wavelength dependence of reflectivity using both images with 4 km-am^{−1} methane absorption coefficient. The ratio of both images is remarkably correlated with the discrete clouds. Where the clouds are brightest, the ratio is close to unity. Where the clouds are absent, the 727-nm image is about 2.4 times as bright as the 888-nm image. This suggests that Neptune’s reflectivity in both images is dominated by two components, a background component with a strong wavelength dependence and a discrete cloud component with a negligible wavelength dependence. The analysis suggested that both components add linearly in reflectivity.

By requiring that the background component is as smooth as possible, we found the wavelength dependence λ^x with exponents $x = -3.7 \pm 0.3$ for the background and 0.1 ± 0.2 for the discrete clouds. The exponent for the background is consistent with the value of -4 for Rayleigh scattering, although stratospheric aerosols may shift this value a little toward -3 , which is the exponent for

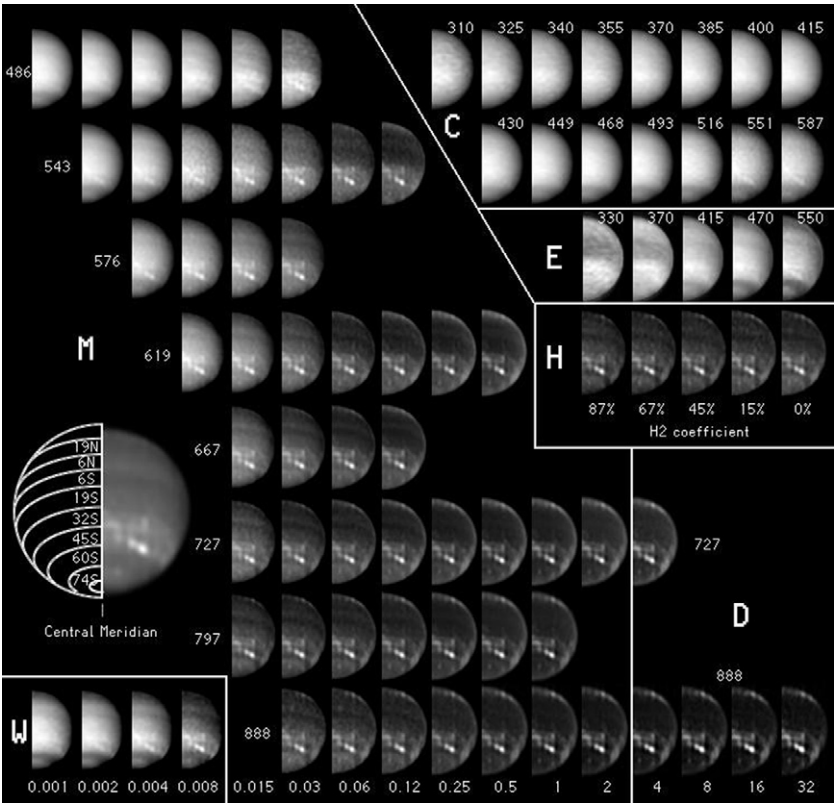


Fig. 2. Observations in our 75 spectral bands. The main panels “M” and “D” show the 55 images in methane bands, ordered according to wavelength (top to bottom) and methane absorption coefficient (left to right). The four weakest methane absorptions, averaged in wavelength, are displayed with enhanced contrast in panel “W”. At the right-hand side are continuum images “C”, with enhanced contrast “E”, and hydrogen absorption images “H”. At the left-hand side is a magnified version of a contrast enhanced image for the spectral band of the human eye with our eight latitudinal regions labeled.

aerosols of roughly $0.1 \mu\text{m}$ radius. The exponent of zero for discrete clouds requires aerosols to be much larger than the wavelength.

Using these exponents, we separated both components by displaying weighted differences of the 727- and 888-nm images in Fig. 3. Above the zero line, the distribution of the reflectivity of discrete clouds is displayed as function of μ , the cosine of the emission angle, and of latitude. Below the zero line on the left side of Fig. 3, the data points mark the background on a negative scale. The sloping line is the best fit with a Minnaert exponent of 0.25, corresponding to the reflectivity proportional to $\mu^{-0.5}$. The scatter of the data points around the fitted line is 0.004, which corresponds to a noise of 0.003 for each image. In areas without discrete features, the noise is half as much.

Using this noise value, we find that 20% of the pixels on Neptune's disk were consistent with the background reflectivity, 80% had discrete clouds. The right panel of Fig. 3 shows discrete clouds concentrated around -40° and $+30^\circ$. The curve of the latitudinal averaged data points has the left concentration double peaked, which is caused by the two very bright features at -50° and several moderately bright features around -35° . The latitude region around $10\text{--}15^\circ$ is completely devoid of discrete clouds, and latitudes near -72° , -58° , and 45° , are almost as bland. All latitudes with the curve significantly above zero show increased scatter, suggesting that at least part of the increased reflectivity is caused by discrete clouds. While the latitudinal distribution of discrete features has changed considerably (Hammel and Lockwood, 1997, 2007; Sromovsky et al., 2001b), our general profile with maxima between -50° and -30° and around 30° latitude and a minimum near the equator seems to be typical.

We found that the few data points near -40° below the zero level were all close to and eastward or westward of bright discrete clouds. They are due to imperfect deconvolution. Since we moved the slit in the opposite direction as the rotation of Neptune, moving features have sharper east–west profiles than the PSF, which causes some overshooting after deconvolution.

We investigated the background reflectivity for the other three spectral bands of panel D in Fig. 2 using the areas of no discrete clouds. We found that the same Minnaert exponent of 0.25 works for all of them, and that the intensity level decreases with increas-

ing methane absorption coefficient, as one might have expected. We subtracted the background reflectivity to analyze the reflectivity of discrete clouds and their ratios. Fig. 4 displays ratios for pixels above the bottom dashed line of Fig. 3, because ratios of smaller reflectivities were noisy.

The left most panel of Fig. 4 confirms that discrete clouds on average have no significant wavelength dependence between 727 and 888 nm. Further to the right, the displayed ratios drop more and more, especially for pixels near the limb, corresponding to small values of μ . We did several statistical tests whether there are significant differences in the ratios between different latitudes, but found only one significant result: Pixels on the northern hemisphere have a significantly higher ratio than pixels in the southern hemisphere for the same μ . We suspect that this transition occurs at the clear region around 10° latitude.

3.2. Interpretation

We used our vertical methane profile of Section 5 to locate the discrete clouds in altitude. In the selected five spectral bands we only see features down to about the 1.3-bar level. A two-way vertical pass to the 1.4-bar layer has already an optical depth of two or more in methane absorption. All data points plotted in the two right-most panels of Fig. 4 have ratios above 0.7 near $\mu = 1$ and above 0.5 near $\mu = 0.5$, indicating that the methane abundance above the scattering aerosols was less than $\frac{1}{2} (-\ln 0.7)/28 = 0.006 \text{ km-am}$ ($\frac{1}{2}$ comes from the double pass, $-\ln 0.7$ is the optical depth, and 28 is the difference in methane absorption coefficients). This locates the aerosols above the 0.6-bar layer, and probably above the 0.4-bar layer considering that the very lowest data points in Fig. 4 are probably due to noise. Thus, we do not see any light scattered from altitudes between the 0.4 and 1.3 bar layers.

Assuming single scattering from the cloud top, our best fits to the data in Fig. 4 are shown as curves, indicating cloud-top levels at a methane abundance of 0.0026 ± 0.003 and $0.0017 \pm 0.005 \text{ km-am}$ for southern and northern clouds, respectively. For our methane model (cf. Section 5), this corresponds to levels of 0.11 and 0.035 bars, respectively. However, others methane mod-

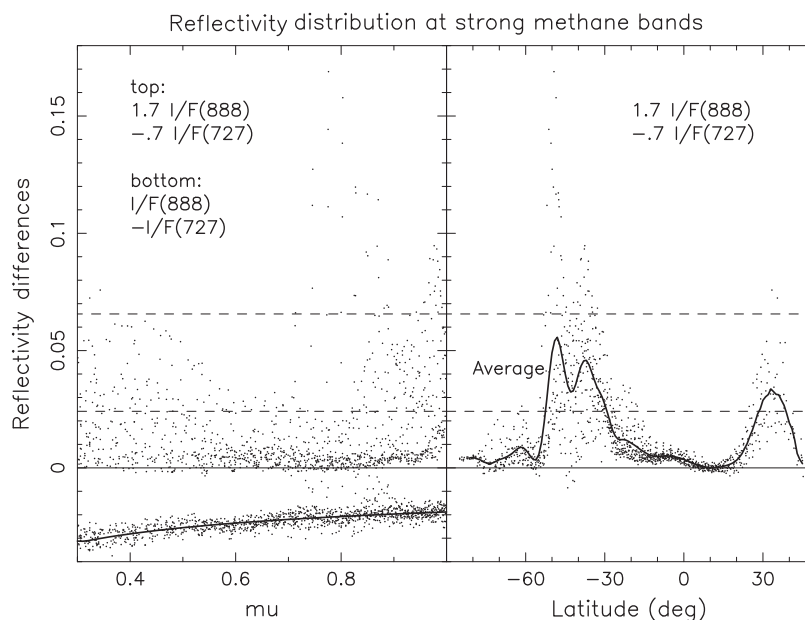


Fig. 3. Reflectivity differences between the two images for 4 km-am^{-1} methane absorption coefficient as function of μ (left) and as function of latitude (right). Data points above the bottom dashed line are used for Fig. 4. Data points above the top dashed line are excluded from center-to-limb fits. Curves indicate a fit to the data (lower left) and latitudinal averages (right).

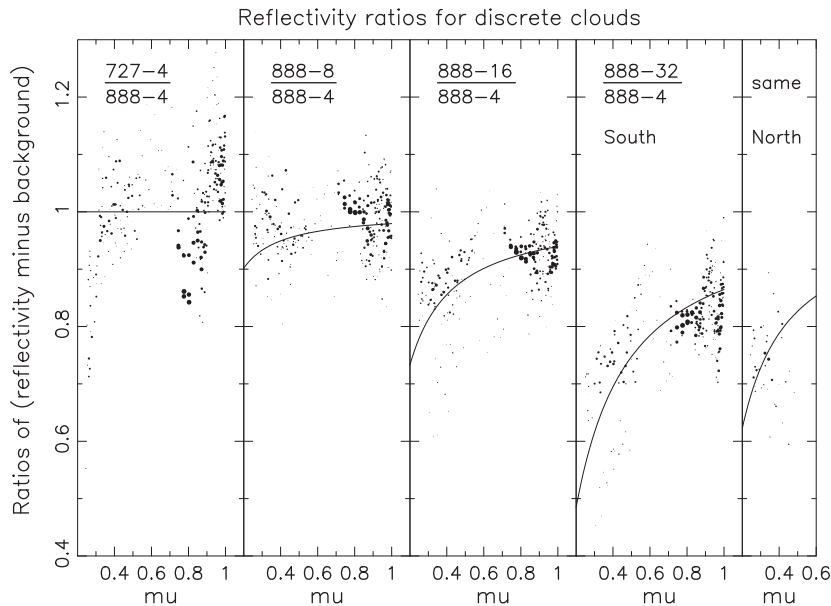


Fig. 4. Ratios of the background subtracted reflectivities between two spectral bands for all pixels above the bottom dashed line of Fig. 3. The spectral band for the denominator is always the 888-nm methane band at 4 km-am^{-1} absorption coefficient. The data for absorption coefficient 32 km-am^{-1} is separated for pixels on Neptune's southern and northern hemisphere. Curves indicate adopted fits assuming 0.0026 km-am methane above the cloud top, except 0.0017 km-am in the panel furthest to the right. The brightest clouds have the largest dots.

els within uncertainties give a wide range of levels within 1.5 scale heights of the tropopause (0.13 bars). Northern clouds are roughly one scale height higher than the southern clouds, unless the observed variation is due to a latitudinal variation of the stratospheric methane abundance. If the discrete clouds are vertically extended, our data probe average altitudes in the optically thin case, or altitudes where the optical depth is around 0.5 in the optically thick case.

Our altitude levels for the discrete clouds are very similar to those obtained from Gibbard et al. (2003) using spectroscopic data near $2 \mu\text{m}$ wavelength at a few slit locations on Neptune's disk. They also found northern clouds to be located at higher levels than southern ones, and by about a similar amount as our results. However, they assumed a larger stratospheric methane mixing ratio. Thus, their methane abundance above the clouds is higher than ours.

Our altitude levels for discrete clouds are higher than those obtained by Sromovsky et al. (2001b) for a northern cloud (0.06 ± 0.02 bars) and two southern clouds (0.19 and 0.23 ± 0.04 bars). Using their assumed stratospheric methane model, we calculated their observed methane abundances above the clouds, which are remarkable similar to ours, 0.0017 km-am for the northern one (same as ours), and 0.0025 and 0.0027 km-am for the two southern clouds versus our average of 0.0026 km-am . These good matches indicate stability of the stratospheric methane abundance and of the processes forming discrete clouds.

Near -22° latitude, our analysis gives enhanced reflectivities with respect to the darkest latitudes (Fig. 4, right panel), which have the typical spectral characteristics of southern clouds, although the images do not show obvious discrete clouds. We concluded that the enhanced reflectivities are due to faint discrete clouds. On the other hand, Pryor et al. (1992) and Baines and Hammel (1994) concluded that the -30° to -22° latitude region had a methane haze around 1 bar with optical depths enhanced by factors of 7–20 with respect to the global mean, while our model does not even show a 10% enhancement of tropospheric haze (cf. Section 6). Note that Pryor and Baines assumed the upper troposphere to be clear. If the upper troposphere had similar opacity as for our

discrete clouds, the best their model could account for was putting the opacity into the methane haze layer.

Between -15° latitude and the equator, Fig. 3 indicates reflectivities enhanced by about 0.004, even less than the 0.01 enhancement near -22° latitude. While the data in each pixel is noisy, this latitude region as a whole shows similar dependence with wavelength and methane absorption coefficient as southern clouds. Thus, even this minuscule enhancement is due to large aerosols at the level of southern clouds. On the other hand, the 10 – 15° latitudes are very clear and cannot have more than half of the clouds of the -15° to 0° latitude region. Otherwise the background would need to have a wavelength dependence steeper than λ^{-4} , which is impossible.

Our result that the two components, background and discrete clouds, add linearly, is consistent with the interpretation that each pixel has a variable fraction of optically thick clouds within its $\sim 2000 \text{ km}$ area probed. We call this fraction the filling factor. We used radiative transfer models, similar to those described in Sections 5 and 6, to compare the characteristics of two cases, an optically thick cloud with a filling factor of 0.05, and a haze with optical depth of 0.05 with unity filling factor. The spectral characteristics were too similar to clearly distinguish both cases. Thus, our term “discrete clouds” applies to all large aerosols at similar altitudes, which could include a smooth, optically thin haze. The key parameter to easily distinguish both cases is the center-to-limb variation of reflectivity. However, the variability of discrete clouds on the time scale of hours (Smith et al., 1989) does not allow center-to-limb observations of the same discrete cloud. Since Voyager 2 images suggest that discrete clouds are generally small compared to the size of our PSF, we adopted the model of optically thick clouds with small filling factors.

We have some constraints on the reflectivity of the clouds. First, the left panel of Fig. 4 indicates that on average, the reflectivity is constant between 727 and 888 nm wavelength. Images in the visible with a background reflectivity of 0.8 indicate small, but still positive contrasts for discrete clouds, indicating a cloud reflectivity near 0.9. We adopted this number.

3.3. Photometric model

Putting all results together, our photometric model is:

$$I/F(x, y, \kappa, \lambda) = 0.9f(x, y) \exp[-2\kappa w/\mu(x, y)] + [1 - f(x, y)]B(x, y, \kappa)\mu(x, y)^{-0.5}\lambda^{-3.7} \quad (1)$$

where $f(x, y)$ is the filling factor as function of both spatial coordinates x and y across Neptune's disk, κ is the methane absorption coefficient in km-am^{-1} , w the methane abundance above the cloud top, 0.0026 km-am for southern and 0.0017 km-am for northern latitudes, and B is the background reflectivity normalized to the disk center and to 1 nm wavelength. We used this model to determine the parameters in the following order.

First, we used the observed reflectivities for the two images at 4 km-am^{-1} methane absorption coefficient, at 727 and 888 nm wavelength. For each position on the disk, there are two equations, one for each wavelength, and two unknowns, $f(x, y)$ and $B(x, y, \kappa)$. Multiplying both equations by $\lambda^{3.7}$ and then subtracting them from each other gives one equation for $f(x, y)$, which then is used in either equation to determine $B(x, y, \kappa)$. Since the small spatial variations of $B(x, y, \kappa)$ calculated this way are probably due to noise, we used its disk average to find the filling factor from each equation, and adopted the mean of both numbers as our filling factor.

Using Eq. (1) one can verify that the positive data displayed in Fig. 3 are within 15% of the filling factor, and the negative data are identical to the background at 888 nm. Thus, the maximum filling factor was about 20%, and the disk average was 1.7%, which is within the range of 0.5–2.3% reported by [Sromovsky et al. \(2001a\)](#) for different dates between 1977 and 1996. At the strongest absorption (32 km-am^{-1}), half of the 0.026 geometric albedo was

due to the background, half due to discrete clouds, and the brightest discrete clouds were 10 times as bright as the background.

With the filling factor determined, we used Eq. (1) to calculate the background reflectivity $B(x, y, \kappa)\mu(x, y)^{-0.5}\lambda^{-3.7}$ for all 75 spectral bands. We call this method the subtraction of discrete clouds, although it is not strictly a subtraction of reflectivity because of the factor $[1 - f(x, y)]$. This method worked remarkable well in canceling out cloud features for the spectral bands taken with the G750L grating (wavelengths 540–1000 nm). Features plotting below the upper dashed line in Fig. 3 became essentially invisible, and the remaining features had positive or negative contrasts about a factor 10 below the original contrast.

Observations using the G430L grating showed mostly different discrete clouds due to Neptune's rotation during the 1–2 h time interval. We used the 540-nm methane band, which was observed with both gratings, to estimate the filling factor in each pixel for the G430L data and then tried the same method of subtraction. We had to reduce cloud reflectivity toward the ultraviolet and roughly account for the extinction of the stratospheric haze to improve the method, which was not critical since discrete clouds have low contrasts below 540 nm wavelength.

The data with clouds subtracted show a Neptune that has not been seen before as clearly as here (Fig. 5), very different from the original images in Fig. 2. Such subtracted images are almost impossible to obtain without an image cube. Our method applied to two images of Neptune generally produces two equations for three unknowns, or by adding another image three equations for four unknowns, since the quantity $B(x, y, \kappa)$ would not be constant. Only the availability of data for different wavelengths and identical methane absorption coefficients in our image cube made our method work. The images of Fig. 5 are the basis for analyzing all the other features of Neptune, which we report in the follow four sections.

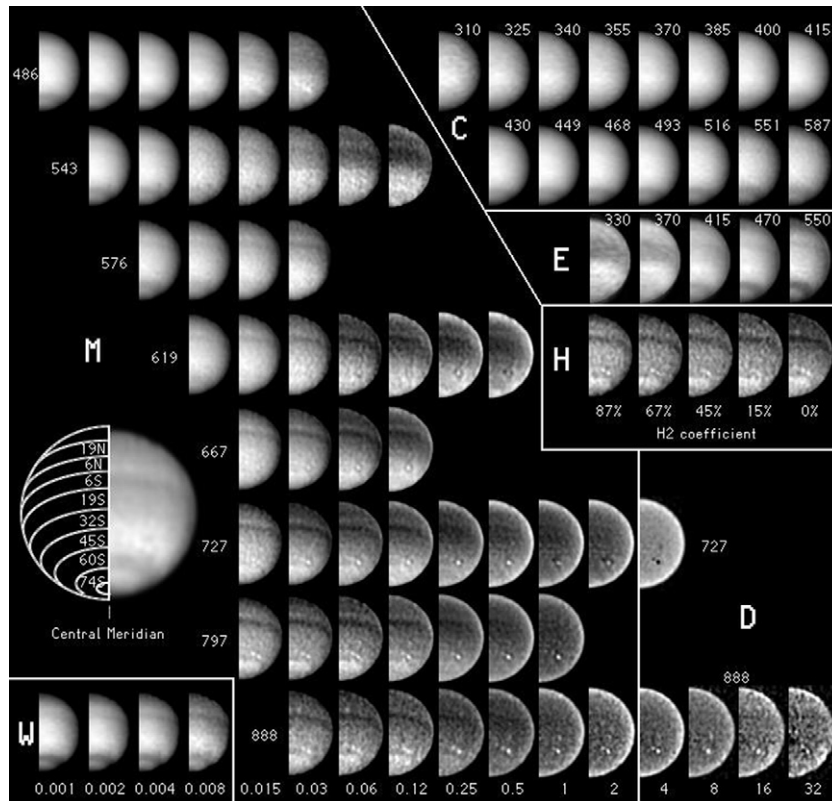


Fig. 5. Observations in our 75 spectral bands with discrete clouds “subtracted”. The layout is similar to Fig. 2.

4. Latitudinal structure

4.1. Center-to-limb fitting

We used the images of Fig. 5 to determine latitudinal and center-to-limb variations with the same technique as in K&T2009. We excluded the 5% of pixels of the strongest discrete features, the data above the top dashed line in Fig. 3, for which the subtraction of discrete features did not work perfectly, as a few spots visible in the images of Fig. 5 indicate.

Our method provided fitted reflectivities at $\mu = 0.4, 0.6$, and 0.8 , called I_4/F , I_6/F , and I_8/F , respectively, and the ratio I_8/I_4 is a measure of limb darkening (center-to-limb variation). While latitudes -81° to 25° included data at $\mu = 0.4$ and 0.6 , only those of -65° to 9° included data for $\mu = 0.8$. We restrict most of our results to roughly these latitude ranges.

We sampled Neptune in 2° latitude steps between -84° and 40° latitude, which includes 98% of all pixels on the disk. This sampling preserved the spatial resolution, $\sim 5^\circ$ at the center of the disk, but was noisy at wavelengths of low signal. Eight wider, representative latitude regions provided data of low noise (Table 2). The final sampling reduced the data cube of 4.4 million data points (2500 pixels on Neptune, 1750 wavelengths) to a set of 210 data points for each latitude, three reflectivities (I_4/F , I_6/F , and I_8/F) in 70 spectral bands, which are all 75 spectral bands minus the five bands used in Section 3 (Table 2).

4.2. Methane absorptions

In the left panel of Fig. 6 we display the latitudinal structure of the reflectivity at 13 different methane absorption coefficients. All methane bands that contained a specific absorption coefficient were averaged, except for the continuum which was taken at 516 nm wavelength. Neptune displays three main features, which are also evident in Fig. 5, a dark band near -60° latitude at the weakest methane absorptions, another dark band near -6° with a sharp northern edge at intermediate methane absorptions, and a general darkening from mid to low southern latitudes at intermediate methane absorptions. These features have reflectivity variations on the order of 10%, which is 100 times less than the brightest discrete clouds in strong absorptions. Thus, accurate accounting of the reflectivity of discrete clouds is essential for measuring other, subtle features.

The relative decrease of reflectivity from one curve to its lower neighbor is directly related to the average amount of methane the reflected light encounters on its path through the atmosphere. Using Eq. (3) of K&T2009, we plot the methane abundance along the path in the center of Fig. 6. Light goes through more methane

at low latitudes than at high southern latitudes, at least for weak absorptions probing lower altitudes.

The spacing of these curves indicates that the probed aerosol opacity is very spread out in altitude, which is the case for a haze model, for example. A reflective layer model would have all curves on top of each other. A two-cloud model would have several curves crowded at two distinct methane abundances. The center-to-limb variation (right panel of Fig. 6) is also indicative of the vertical aerosol distribution. A reflective layer model has methane abundances inversely proportional to μ , while the observations show them closer to proportional to μ , which is roughly that of haze models.

The largest methane abundance along the path in Fig. 6 is 60 km-am, and its maximum may be around 70 km-am at even weaker absorptions, which requires light typically to be reflected from layers around 15–25 bars, somewhat dependent on the type of model and the methane mixing ratio. On the other hand, the reflective layer at 3.8 bars in models by Baines et al. (1995) and Sromovsky et al. (2001b) would have limited the methane abundance along the path to 8.6 km-am. Clearly, this reflective layer does not exist. Note that their models were based on data for stronger absorptions, for which we also observe methane abundances along the path below 8.6 km-am. Thus, their models may still be suitable for interpreting stronger absorptions, but the reflective layer at 3.8 bars was an assumption that is contradicted by our observations.

The center panel of Fig. 6 looks similar to the left panel of Fig. 11 of K&T2009, which shows the same quantity for Uranus. The curves for the weak absorptions are generally some 20% lower for Uranus than for Neptune, which is small compared to the vertical scale extending over a factor of ~ 30 . Also, the general slope of the upper curves is a somewhat stronger for Uranus than for Neptune. Small scale features, such as local minima near -45° for Uranus or -70° for Neptune are quite different on both planets.

Note that the mentioned 70 km-am methane abundance is 80,000 times larger than the methane abundance difference of 0.0009 km-am between southern and northern clouds (Section 3.2), which indicates the broad range of absorptions probed by our observations.

4.3. Hydrogen absorptions

On Neptune, collision induced hydrogen absorption dominates methane absorption only in a very small part of our spectral range, between 820 and 832 nm wavelength (thick bar in Fig. 7). In this spectral region, Neptune's geometric albedo spectrum follows the shape of hydrogen absorption, while it otherwise follows the shape of methane absorption. The reflectivity ratio between Neptune's southern and northern half of the disk is mostly correlated with

Table 2
Spectral bands and latitude regions.

Continuum wavelengths (panel C of Figs. 2 and 5, left panel of Figs. 11–13): 15 bands centered at 310, 325, 340, 355, 370, 385, 400, 415, 430, 449, 468, 493, 516, 551, 587 nm								
Methane bands (panel M of Figs. 2 and 5, central panels of Figs. 11–13): 50 spectral bands for eight methane bands and several methane absorption coefficients every factor of two								
Band (nm)	486	543	576	619	667	727	797	888
Minimum coefficient (km-am ⁻¹)	0.001	0.002	0.004	0.008	0.015	0.015	0.015	0.03
Maximum coefficient (km-am ⁻¹)	0.03	0.12	0.03	0.5	0.12	2	1	2
Hydrogen absorptions (panel H of Figs. 2 and 5, right panel of Figs. 11–13): five bands of 16 spectral pixels each near 826 nm with average relative hydrogen absorption coefficients of 87%, 67%, 45%, 15%, and 0%. The last band averages data near 740 and 930 nm. Neptune's geometric albedo was 0.155 in each band								
Strong absorptions (panel D of Figs. 2 and 5, Fig. 4): the 727 nm methane band at 4 km-am ⁻¹ methane absorption coefficient and the 888 nm methane band at 4, 8, 16, and 32 km-am ⁻¹								
Latitude regions (planetographic latitudes): eight regions with the following widths								
Region name	74S	60S	45S	32S	19S	6S	6N	19N
Minimum latitude (°)	-79	-67	-51	-38	-25	-11	1	13
Maximum latitude (°)	-69	-53	-39	-26	-13	-1	11	25

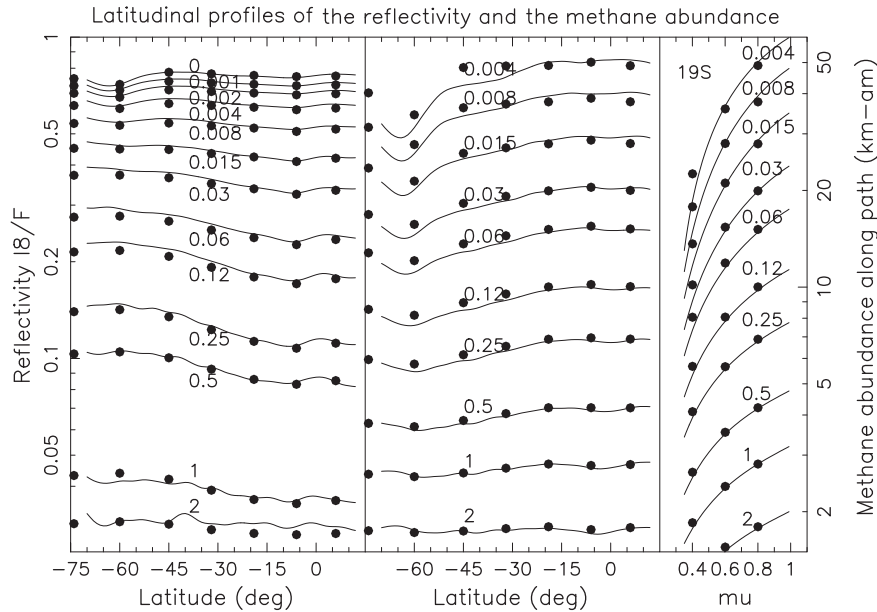


Fig. 6. Reflectivity I_8/F (left) and methane abundance along the path (center) as function of latitude for observations (curves) and adopted models (dots). The labels indicate the methane absorption coefficients in km-am^{-1} . The right panel shows the methane abundance along the path for latitude region 19S as function of μ .

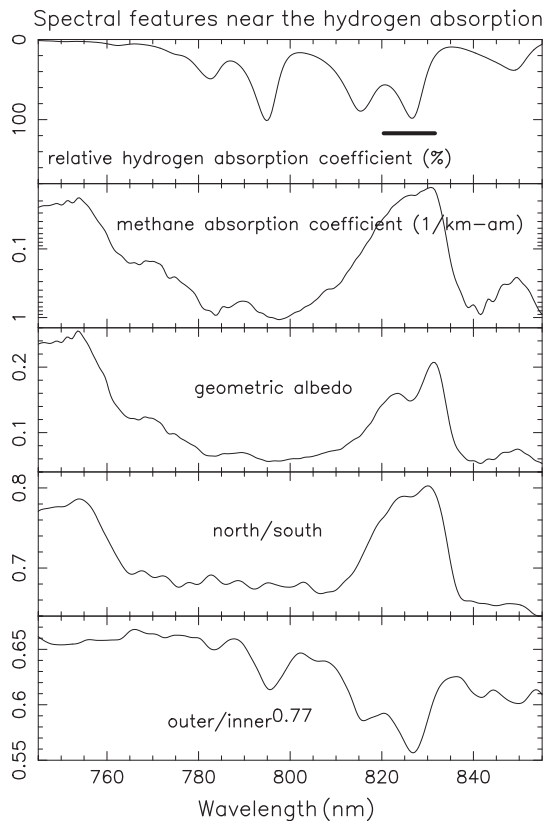


Fig. 7. The spectral shape of the hydrogen absorption coefficients at 70 K temperature and methane absorption coefficients compared with Neptune's geometric albedo, the reflectivity ratio between the southern and northern half of the disk, and the reflectivity ratio between the outer half of the disk and the inner half raised to the power 0.77.

the methane spectrum (fourth panel of Fig. 7). This indicates that the asymmetry is due to methane and not due to aerosol opacity. Dividing the disk into inner and outer halves (equal disk areas),

the ratio $(\text{outer half})/(\text{inner half})^{0.77}$ is mostly correlated with the hydrogen spectrum. This indicates that the hydrogen absorption is well observed. Our data set is the first observation of spatial variability of this hydrogen absorption, and simple ratios suggests that our current view of Neptune, a methane mixing profile independent of latitude, is wrong.

The left side of Fig. 8 displays reflectivity profiles in our five spectral bands that have the same geometric albedo of Neptune, but absorption coming from methane (0% curve) to mostly hydrogen (87% curve). The display is similar to the left side of Fig. 13 in K&T2009 for Uranus.

Southward of -45° and northward of -20° latitude, all curves are roughly parallel to each other. Thus, the features seen are mostly due to features in aerosol optical depth. In between, there is a consistent variation of the slope from curves probing methane to those probing mostly hydrogen absorption. This is indicative of a variation of the methane mixing ratio.

Models of Section 6 indicate that the solid curve (87%) indicates features of aerosol optical depth, because it is almost independent of the methane mixing ratio. Wherever the methane mixing ratio increases, the mean molecular weight increases too. This decreases the hydrogen density and thus the hydrogen absorption, which happens to just balance the increase of methane absorption. The solid curve indicates a maximum aerosol opacity near -65° and a minimum near -5° latitude, with almost constant opacity between -55° and -20° .

The top half of the right panel in Fig. 8 shows probed methane and hydrogen abundances by the observations, similar to the left side of Fig. 14 of K&T2009 for Uranus. At mid-southern latitudes of Neptune, where methane and hydrogen curves have opposite slopes, the main cause must be a variation of the methane mixing ratio. Toward the left and right, where curves go roughly parallel to each other, the features are mostly due to aerosol opacity. This is consistent with the conclusion derived from the left side of Fig. 8.

On the bottom right of Fig. 8 we repeated the method described in K&T2009 (second half of their Section 3.4) to estimate the latitudinal variation of the relative methane mixing ratio and show results for Uranus and Neptune (solid curves). On both planets, the mixing ratio seems roughly constant at high southern and at low latitudes with a transition at mid-southern latitudes. The variation

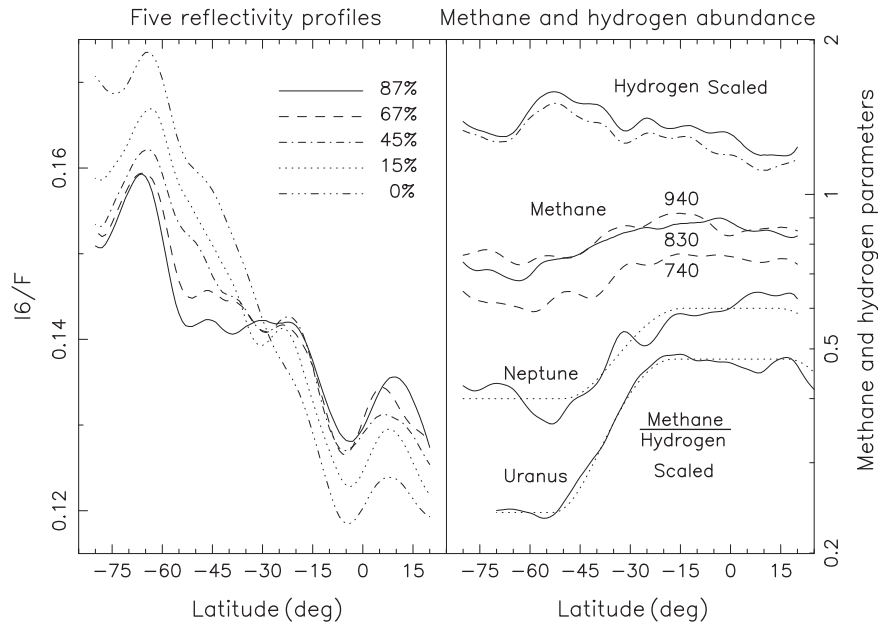


Fig. 8. Left panel: reflectivity I_6/F as function of latitude for five spectral bands near the 826-nm hydrogen absorption with the relative strength of the hydrogen absorption indicated. Right panel top: methane abundance along the path for three methane windows and an analog parameter for the hydrogen absorption as function of latitude, all on a relative scale. Right panel bottom: the ratio of methane and hydrogen abundance probed as function of latitude for Uranus and Neptune, on a relative scale as well (solid curves). The dotted curves are fitted functions.

is stronger on Uranus, a factor of ~ 2 versus ~ 1.5 for Neptune. Neptune's values are higher than Uranus' at all latitudes, which may indicate higher mixing ratios, but this conclusion may be premature since the light probes different levels on both planets. K&T2009 fitted the latitudinal variation with a sine curve between -53° and -17° latitude and constant otherwise (dotted curve). For Neptune, the best fit (dotted curve) has the sine curve shifted by 3° (-50° to -14°), but such a small difference is not significant. The fit is not as good as for Uranus, which we attribute to the larger noise of the Neptune data.

4.4. Continuum

Fig. 9 shows the latitudinal variation of the continuum reflectivity in a similar way as Fig. 16 of K&T2009 for Uranus, except that one tick mark is 2% for Neptune while it was 1% for Uranus. In the ultraviolet, both planets have essentially the same features, a local minimum at the equator or just south of the equator, and a local maximum at mid-southern latitudes, although the maximum is close to -30° on Uranus and -40° on Neptune. The general gradient from the northernmost to the southernmost probed latitudes

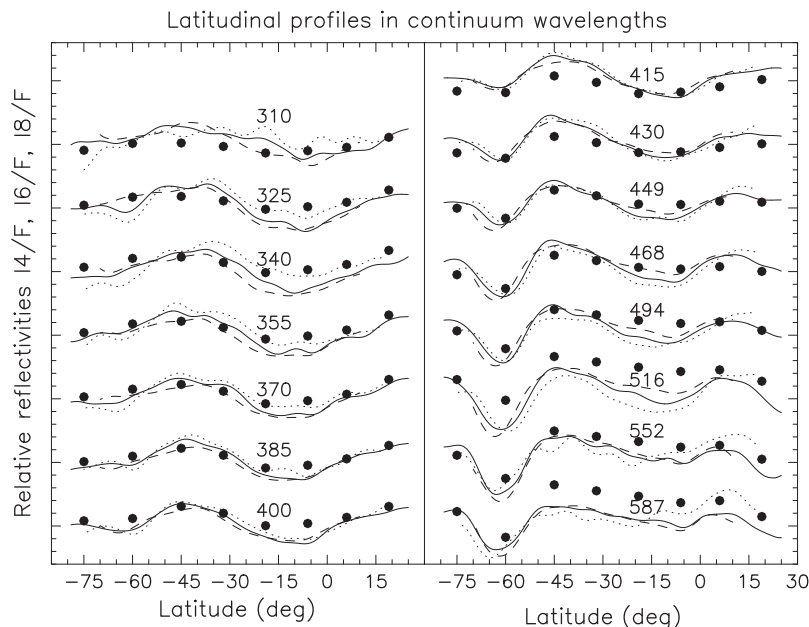


Fig. 9. Latitudinal profiles of the reflectivity I_4/F (dotted), I_6/F (solid), and I_8/F (dashed) in our 15 continuum spectral bands from the observations, and adopted models for I_6/F (dots). Each curve was normalized to a latitudinal average at the large tick marks. Large and small tick marks are separated by 10% and 2% in reflectivity, respectively.

is larger on Uranus than on Neptune. In the visible continuum, contrasts on both planets are quite muted, except for an obvious dark band near -60° latitude on Neptune. This dark band has been consistently observed over many years (cf. discussion and references in [Sromovsky et al. \(2001b\)](#)).

While [Figs. 5–9](#) allowed qualitative statements about the latitudinal aerosol and methane variations seen on Neptune, we discuss radiative transfer models in the following two sections to put these results on a quantitative footing.

5. Model setup

5.1. Composition of atmosphere

We used the same radiative transfer code as in [K&T2009](#) for Uranus, but adjusted the parameters in the following way. For Neptune, we used the calculated gravity at each latitude, which varies between 11.0 and 11.4 m s^{-2} from equator to pole ([Lindal, 1992](#)). For the composition of the atmosphere, we used a 19:81 mixing ratio of helium to hydrogen from [Conrath et al. \(1991\)](#). [Conrath et al. \(1993\)](#) considered the possibility of a mole fraction of 0.003 for nitrogen with a helium mole fraction of ~ 0.15 that was favored by [Burgdorf et al. \(2003\)](#). This possibility would give almost identical model reflectivities for all our spectral bands.

The distribution of the third most abundant species, methane, is connected to the vertical temperature structure. We adopted the temperature profile by [Lindal \(1992\)](#), who assumed a constant methane relative humidity down to the ~ 1.9 bar level and a constant methane mixing ratio of 0.02 ± 0.02 at lower altitudes. We used a similar approach for low latitudes, up to $\pm 14^\circ$, where we see the maximum amount of methane.

We assumed stratospheric and tropospheric methane mixing ratios (mole fractions) of 0.0006 and 0.04, respectively, except where such a mixing ratio would correspond to a methane relative humidity above 60%. At those altitudes, between the 0.035- and 1.8-bar layers, the humidity was set to 60%. The tropospheric methane mixing ratio was based on our comparison between models and observations for the relative strength of methane and hydrogen

absorptions, which only gave good fits for methane mixing ratios between 0.03 and 0.05. Values slightly outside this region may be also allowed considering uncertainties of absorption coefficients. We started with a humidity value of 20% from the assumed value by [Lindal \(1992\)](#), but realized that we had to double it at least to get good fits. Values between 40% and 100% can be accommodated by our constraints. Values other than 60% would shift some parameters slightly. A latitudinal variation of the methane relative humidity by more than a factor of two in the ~ 0.5 – 1.5 bar region would show up as a detectable feature in the background reflectivity at the strongest methane absorptions. None was detected.

Our methane mixing ratio of 0.0006 for the stratosphere is the lower limit of the range 0.0006–0.005 by [Yelle et al. \(1993\)](#), which is in between values of 0.00035 favored by [Baines et al. \(1995\)](#) and 0.0017 by [Gibbard et al. \(2003\)](#). This parameter is significant for locating discrete clouds (Section 3), but is completely insignificant for the tropospheric structure studied here. The right side of [Fig. 10](#) displays the temperature profile from [Lindal \(1992\)](#) and our adopted methane profile for low latitudes ($6S$). The dashed line shows the profile on a 10 times expanded scale. For higher latitudes we modified the methane profile according to our analysis described later.

5.2. Aerosol properties

For Neptune, we adopted the stratospheric aerosol properties of [K&T2009](#) for Uranus, aerosols with mean radii of $0.1 \mu\text{m}$ calculated with Mie scattering theory, similar to the $\sim 0.13 \mu\text{m}$ radius inferred by [Moses et al. \(1995\)](#) from high phase-angle Voyager imaging, but smaller than the $0.2 \pm 0.05 \mu\text{m}$ value inferred by [Pryor et al. \(1992\)](#) from high phase-angle Voyager PPS data.

We adopted the following single scattering albedo of Neptune's tropospheric aerosols, dependent on the wavelength λ (nm) and the latitude ϕ :

$$\tilde{\omega}_t(\lambda, \phi) = \tilde{\omega}_0(\phi) - \tilde{\omega}_1(\phi) / \{2 + \exp[(\lambda - 290)/30]\}. \quad (2)$$

The parameter $\tilde{\omega}_0(\phi)$ gives the single scattering albedo as the wavelength goes toward the near infrared, while the parameter $\tilde{\omega}_1(\phi)$ is a measure for the spectral slope of the single scattering albedo in

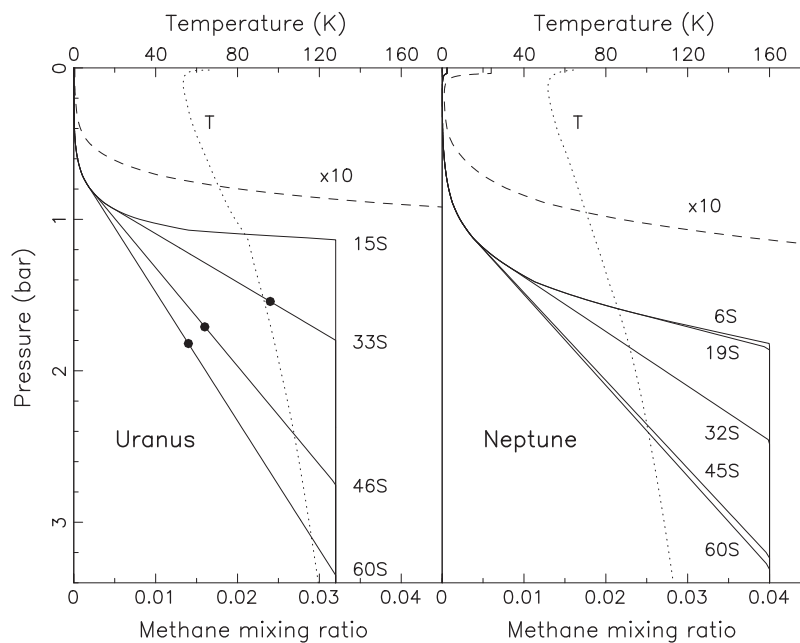


Fig. 10. Proposed methane mixing ratio as function of pressure (solid curves) for four latitudes on Uranus (left) and five latitudes on Neptune (right), also shown on a 10 times enhanced scale (dashed). The solid dots on the left side indicate methane mixing ratios by [K&T2009](#). Also shown are the temperature–pressure profiles (dotted) on the scale at top, taken from [Lindal et al. \(1987\)](#) and [Lindal \(1992\)](#).

the ultraviolet. If both parameters are set to unity, the function becomes very close to that adopted by K&T2009 for Uranus. The only difference is a slightly shallower spectral slope for Uranus. For Neptune (cf. Section 6), the best fitting parameter $\tilde{\omega}_0(\phi)$ was very close to unity, while the best fitting parameter $\tilde{\omega}_1(\phi)$ varied between 0.8 and 1.9. We experimented with a number of different kinds of functions for the single scattering albedo, but the adopted functional form gave the smallest residuals.

Our double Henyey–Greenstein phase functions (Henyey and Greenstein, 1941) for tropospheric aerosols have three free parameters: g_1 and g_2 set the magnitudes of the forward and backward scattering peak, respectively, while f_1 sets the fraction attributed to the forward scattering function. The weighted g is typically defined as $f_1 g_1 + (1 - f_1) g_2$. Since our observations were made at 0° phase angle, they are mostly sensitive to the magnitude of the backscattering peak. For Uranus in K&T2009, we set g_1 and g_2 at 0.7 and -0.3 , respectively, and fitted the value of f_1 as function of wavelength based on the observations. This gave realistic back scattering peaks, but unrealistic forward scattering peaks that increased toward longer wavelengths, just opposite to theoretical expectations.

In order to adopt more realistic phase functions for Neptune, we set f_1 and g constant at 0.7 and 0.44, respectively, which are “average” values obtained for aerosols in the outer Solar System, for example $f_1 = 0.76$ – 0.86 for Saturn and 0.42 for Neptune, and $g = 0.39$ – 0.67 for Saturn and 0.31 for Neptune (Tomasko and Doose, 1984; Pryor et al., 1992). We adjusted the third parameter, g_1 , according to the data, which then defines g_2 . This gave the following parameters:

$$g_1 = 0.725 - 0.075 \sin[(\lambda - 680)/2] \quad (3)$$

$$g_2 = -0.225 + 0.175 \sin[(\lambda - 680)/2] \quad (4)$$

between 500 and 860 nm wavelength. Outside this range, both parameters remain at their values at 500 and 860 nm, respectively. The parameter g_1 decreases from 0.8 to 0.65 from the blue to near infrared, while g_2 increases from -0.4 to -0.05 . At 750-nm wavelength, $g_2 = -0.12$, which is within the range of -0.07 to -0.22 determined by Pryor et al. (1992). Our phase functions for Neptune and Uranus (K&T2009) have both backscattering peaks that are weak at long wavelengths and strong at short wavelength with most of the transition occurring between 500 and 800 nm. We found no evidence for a variation of the phase function with latitude, nor with altitude, and thus the same phase function was adopted throughout Neptune’s troposphere.

Observed variations of continuum reflectivities with latitude may be caused by a variable single scattering albedo or by a variable backscattering peak of the phase function. Only in the former case does the contrast of the observed banding structure weaken from the center of the disk to the limb, which our data indicated. Thus, we adopted a constant phase function and fitted the single scattering albedo to the data as function of latitude.

Observations at $>28 \mu\text{m}$ wavelength by Burgdorf et al. (2003) indicated aerosol radii of 15–40 μm that have constant optical depths at wavelengths below 1 μm . Thus, we adopted the result of wavelength-independent optical depths for the tropospheric aerosols.

6. Vertical structure

6.1. General structure

Generally, results for the vertical distribution of aerosols from methane band observations are very dependent on the assumed methane absorption coefficients. Small changes in the coefficients within their uncertainties give very different best-fitting models. Therefore, in K&T2009, we presented a method that is independent of the coefficients. We calculated two parameters, such as reflectivities at two center-to-limb locations, for models with all methane absorption coefficients between zero and infinity, which defines a curve in the two-parameter space of both reflectivities. We then checked whether all observed pairs of reflectivities within one methane band plot on top of the curve (within uncertainties). This is a sensitive test of the vertical aerosol structure that does not need any knowledge about methane absorption coefficients. We used the same method here.

We compared haze models containing wide layers of aerosols with cloud layer models where the aerosols are confined to a few narrow layers. Our result for Neptune is the same as for Uranus (K&T2009): haze models produce better fits than cloud layer models with the same number of free parameters. Thus, we divided Neptune’s troposphere in a number of haze layers of about half a scale height width, which is roughly our vertical resolution. We modeled the stratosphere as a single layer since we do not have vertical resolution above the tropopause (0.13 bars).

Our models have the troposphere above the 1.4 bar layer clear (aside from discrete clouds studied and “subtracted” in Section 3) since this provided the best fit to the data in the stronger methane absorptions. Below the 1.4 bar layer, the haze opacity in each layer is described by the optical depth per bar of pressure. Setting this number identical for all layers gave good fits, and thus we adopted this simple model. An equivalent description would be a cloud layer model with 4–5 cloud layers with pressure levels and opacities adjusted to give the same observed opacities within each half a scale height, which is not as simple as our model of a single haze layer.

Our goal of constraining the vertical haze structure as function of latitude has two components. First, we investigated reflectivities of a particular latitude. Second, we investigated observed latitudinal variations of reflectivities. Since uncertainties deriving from methane absorption coefficients are generally many times larger than observational uncertainties, the accuracy of the first component is mostly limited by our current knowledge of methane absorption coefficients. The second component can be much more accurately constrained since it is only limited by observational errors.

We first analyzed our latitude region 6S because it contains center-to-limb data over almost the full range of scattering geometries, up to $\mu = 0.93$, and it was almost free of discrete clouds. Our model has stratospheric haze with an optical depth of 0.04 times the extinction efficiency (which is unity at 370 nm and 0.1 at 900 nm wavelength), a clear space between 0.13 and 1.4 bars, and a semi-infinite haze layer below with an optical depth of 0.11/bar (Table 3). Other parameters are explained in Section 5 with the two variables set at $\tilde{\omega}_0 = 0.992$ and $\tilde{\omega}_1 = 1.9$. This is our standard model we use for all comparisons in the next section.

Table 3
Aerosol model.

Stratosphere: spherical aerosols of 0.1 μm mean radius, size distribution with 0.3 normalized variance, refractive index $1.4 + n_i i$, cf. Eq. (5) of K&T2009, optical depth 0.04 for unity extinction efficiency (~ 370 nm wavelength) and 0.004 near 900 nm wavelength
Troposphere above 1.4-bar layer: clear except for discrete clouds of 0.9 reflectivity and variable filling factor across the disk at the level of 0.0026 and 0.0017 km-am methane abundance for southern and northern clouds, respectively (near tropopause, cf. Section 3)
Troposphere below 1.4-bar layer: uniform haze, single scattering albedo cf. Eq. (2) with parameters of Fig. 14, double Henyey–Greenstein phase function with $f_1 = 0.7$, g_1 and g_2 , cf. Eqs. (3) and (4), optical depth between 0.10 and 0.16/bar as function of latitude, cf. Fig. 14

Our stratospheric haze optical depth at 750 nm wavelength of 0.007 is smaller than the value of 0.05 ± 0.02 by Pryor et al. (1992). At 265 nm wavelength, our extrapolated value (0.07) is smaller than Pryor's (0.19 ± 0.08). While our data at zero phase angle are mostly sensitive to the absorption optical depth in the ultraviolet, Pryor's data at high phase angle are mostly sensitive to the scattering optical depth. Both results could be made consistent by changing the adopted single scattering albedos. Because of these intrinsic difficulties in determining absolute optical depths, our results are mostly focused on determining latitudinal variations.

6.2. Parameter sensitivity

We changed 12 parameters of our model for latitude 6S, one at a time, to determine which parameters may be responsible for observed latitudinal variations. Even more important, we checked whether we could uniquely identify the parameter(s) responsible, or whether there are families of solutions with different parameter combinations providing the same reflectivities. If each of the 12 parameters causes a spectral signature that is unique compared to the other 11 parameters and combinations of the other parameters, then the observations can constrain that parameter uniquely. If this is not the case, then families of solutions exist. This method is only applicable if latitudinal variations are sufficiently small so that reflectivities change according to linear superposition of the 12 parameters. We confirmed that this is indeed a good approximation for our minor latitudinal variations observed.

Fig. 11 shows the sensitivity of our data to 12 physical parameters. Three curves indicate I_4/F (dotted), I_6/F (solid), and I_8/F (dashed). Black dots indicate zero levels that mean no reflectivity change. A curve one tick mark above the black dots indicates a 5% reflectivity increase with respect to the standard model.

The bottom scale on Fig. 11 has 70 tick marks indicating the 70 spectral bands, first the 15 continuum wavelengths (Table 2, continuum wavelengths, Fig. 2C), then eight panels for the eight meth-

ane bands with every fifth absorption coefficient labeled (Table 2, methane bands, Fig. 2M), and finally the hydrogen absorption with the relative strength labeled (Table 2, hydrogen absorption, Fig. 2H). Within each of the eight middle panels, the quasi-continuum (methane window) is at the left-most tick mark while the band center (largest absorption coefficient) is at the right-most tick mark. The wavelength limits for each methane band are shown in Fig. 5 of K&T2009.

The 12 models are labeled at the right edge of Fig. 11 with a number and a letter. Models that have similar impact on the reflectivities have the same number. Models that have similar parameters changed have the same letter, W for single scattering albedo, S for stratosphere, T for tropospheric aerosol opacity, M for methane mixing ratio, and D for discrete clouds (cf. Table 4).

In 11 of the 12 models, we changed the variable parameter in the direction where most of the model reflectivities increase. This facilitates the comparison between different models. For one model (2W), the variable parameter $\bar{\omega}_0 = 0.992$ was so close to unity that we had to decrease it which gives lower reflectivities. However, we plotted the reverse change (increase from 0.95 to 0.992) for an easier comparison with other models, in particular model 2T.

The top pair of models (1S and 1W) has only ultraviolet reflectivities changed significantly with respect to the standard model. For model 1S with no stratospheric aerosols, the change is strongest near the limb (dotted line). For model 1W with no ultraviolet absorption in the tropospheric haze, the change is strongest near the center of the disk (dashed line) because ultraviolet light from the limb does not probe to the lower atmosphere. Thus, limb darkening data is critical to distinguish between both possibilities.

Model 1S shows that stratospheric aerosols can only be detected at ultraviolet wavelengths and in the strongest methane absorptions (right sides of panels 727–888). Ultraviolet observations are critical since methane bands alone cannot distinguish between models of types 1S and 7D.

The next two models (2W and 2T) mostly change reflectivities in the visible continuum and weak methane absorption (left sides

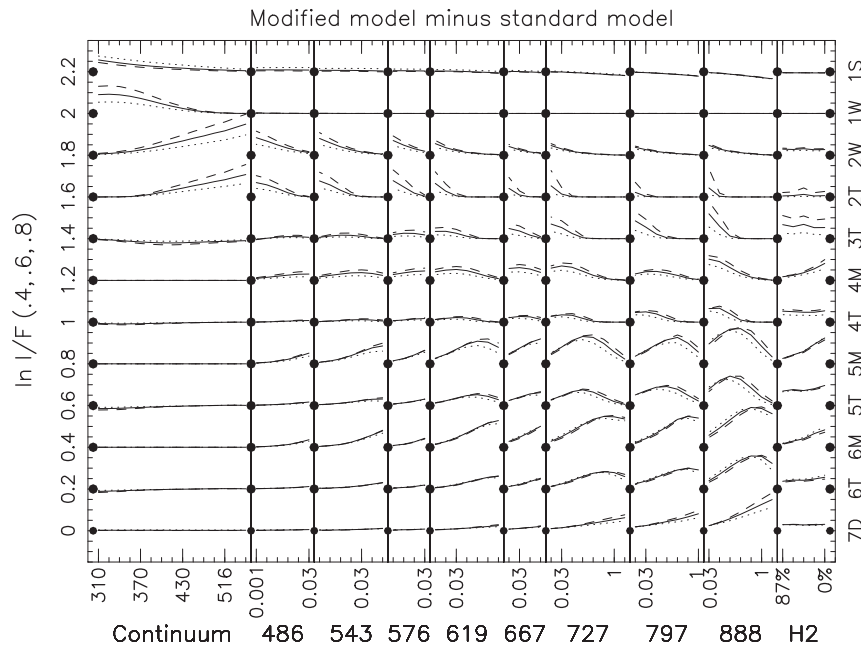


Fig. 11. Signature of changing one of 12 model parameters at a time with respect to our adopted model at latitude region 6S. The 12 cases (right) are described in Table 4. The horizontal scale has one tick mark for each of our 70 spectral bands, the 15 continuum bands (left panel), the eight methane bands (following eight panels) with absorption coefficients labeled, and the five bands near the 826-nm hydrogen absorption with relative hydrogen absorption coefficients labeled (cf. Table 2). Solid dots indicate the zero level for each of the 12 cases. Each case has curves displaced by 0.2 with respect to the next one. One vertical tick mark corresponds to a 5% change of the reflectivity. Dotted, solid, and dashed curves indicate I_4/F , I_6/F , and I_8/F reflectivities, respectively.

Table 4
Non-standard models of Fig. 11 for latitude region 6S.

1S: no stratospheric aerosols
1W: single scattering albedo of tropospheric aerosols constant, $\bar{\omega}_1 = 0$ in Eq. (2)
2W: near infrared single scattering albedo $\bar{\omega}_0 = 0.992$ (standard model) versus 0.95 (changed)
2T: reflective layer of albedo unity at 12 bar pressure
3T: tropospheric aerosol optical depth doubled below 4-bar layer
4M: methane mixing ratio reduced from 0.04 to 0.032
4T: tropospheric aerosol optical depth doubled between 2.5- and 4-bar layers
5M: methane mixing ratio between 1.2 and 3 bars pressure reduced as model at -42° latitude
5T: tropospheric aerosol optical depth increased by 60% between 1.4- and 2.5-bar layers
6M: methane relative humidity reduced from 60% to 30%
6T: tropospheric aerosol upper boundary at 1.1 bars instead of 1.4 bars pressure
7D: reflective layer of albedo unity at tropopause with 0.4% filling factor (discrete clouds)

of panels 727–888). They can only be distinguished at weak near-infrared methane absorptions, where model 2W, a changed single scattering albedo of tropospheric aerosols, has essentially unchanged limb darkening (all three curves plot on top of each other). Model 2T, a reflective layer at 12 bars, shows large changes of the limb darkening considering the large spread between the dashed and dotted curves at the same locations because light from the limb does not probe to the deepest levels. Again, the limb darkening information is needed to distinguish between both cases. A model with a clear atmosphere below the 12 bar level has similar characteristics as model 2T, just of opposite sign. A major opacity structure at 12 bars would be easily detectable since our 1% accuracy for limb darkening is 10 times lower than the deviations of model 2T. No other planet can be probed that deeply at similar wavelengths.

The bottom eight models are characterized by changes of reflectivities in methane bands, but not in the continuum. They are ordered according to the location of maximum change, occurring at weak absorptions (top) to strong absorptions (bottom). Model 3T, the aerosol optical depth doubled below the 4-bar level, can be distinguished from the other seven since it is the only one with a strong change of limb darkening.

The next three pairs (#4–6) have the strongest change at weak, medium, and strong absorptions, respectively. Both models within each pair seem difficult to distinguish. Only the right panel for the hydrogen absorption sets both models apart from each other with curves sloping up (M models) and horizontal curves (T models). The models correspond to changes of the methane profile (M models) and aerosol opacity profile (T models). Clearly, the hydrogen absorption data are critical to distinguish between methane and opacity variations.

The shape of the curves can be qualitatively understood. For example, the 727-nm methane band for model 5T, which has more aerosols in the middle troposphere, produces a similar absolute increase of reflectivity for weak to middle methane absorptions. For the weakest absorptions (left side of panel 727), Neptune's reflectivity is so large that the relative increase in reflectivity is small. For medium absorptions (middle of panel), Neptune's reflectivity is low enough to give a large relative increase in reflectivity. For the strongest methane absorptions (right side of panel 727), light does not probe down to the middle troposphere so that the reflectivity is essentially unchanged.

Finally, model 7D at the bottom of Fig. 11 indicates that the impact of discrete clouds is restricted to even stronger methane absorption coefficients than for the #6 models. Based on these considerations, we feel confident that we can identify the correct

physical parameter among these 12 parameters for observed latitudinal variations, as long as they are well above uncertainties.

6.3. Latitudinal variation

We now investigate the three most prominent latitudinal features discussed in Section 4. The strongest feature is obvious in most methane bands, a dark low-latitude region and a bright southern high-latitude region with a transition near the center of the disk, around -30° latitude. We characterize this feature by plotting the difference of the logarithm of reflectivity between the latitude regions 19S and 45S (top of Fig. 12). The second feature is a narrow dark belt just south of the equator, most prominent in weak to medium absorptions, characterized by comparing the average for latitude regions 19S and 6N with 6S (middle of Fig. 12). The third feature is the dark belt near -60° latitude, apparent in the visible continuum, characterized by 60S versus the average of 74S and 45S (bottom in Fig. 12).

The first feature is best explained by a change of the methane mixing ratio between 1 and 3 bars with very minor changes of other parameters. Qualitatively, the curves peaking at medium methane absorption tell that the change must occur in the middle troposphere; the steep slope in the right-most panel tells that hydrogen and methane absorptions of similar strength behave differently at both latitudes, which requires a change of the methane mixing ratio profile.

The second feature is best explained by a change of the tropospheric haze optical depth, although the dark ultraviolet reflectivities just north of the disk center also require increased ultraviolet absorption for the tropospheric haze. Qualitatively, the lack of change in continuum wavelengths and the zero slope in the right-most panel tell that the main change comes from aerosol optical depth variation between both latitude bands.

The third feature is best explained by a decrease of single scattering albedo of tropospheric aerosols at long wavelengths. Qualitatively, a major change in the visible continuum, where the deepest layers are probed through multiple scattering, could be due to a change of tropospheric aerosol single scattering albedos or a change deep in the atmosphere. The deep atmosphere is much better probed in the center of the disk than near the limb. However, all three curves (solid, dashed, and dotted) are similar indicating a lack of limb-darkening change, which argues for the former explanation.

We investigated other, minor latitudinal features in a similar way and concluded that most of the latitudinal variations can be explained by variations of four parameters, two parameters for the single scattering albedo of tropospheric aerosols at short and long wavelengths (cf. Eq. (2)), one parameter for the optical depth per bar of the tropospheric haze, and one parameter for the decrease of methane mixing ratio in the middle troposphere. Our method determined the four variable parameters for each of our eight latitude regions. These eight models fit our data to 2.8% rms in reflectivity. The residual can only be slightly decreased by allowing further parameters to vary with latitude. For example, the methane absorptions around 1 km-am^{-1} of the 888 nm methane band indicate a pressure level for a top of the tropospheric haze of 1.3–1.4 bar for high southern latitudes but 1.4–1.5 bars for low latitudes. Such a small variation may be real, but our data are insufficient to establish it.

One interesting result is that we included six variable parameters about the vertical haze structure, but that all latitudes revealed a very simple structure with only one variable parameter, the tropospheric haze optical depth, variable with latitude between 0.10 and 0.16/bar. On the other hand, the methane mixing profile is more complicated than anticipated. The spectral characteristics for the variation between 45S and 19S (top of Fig. 12) re-

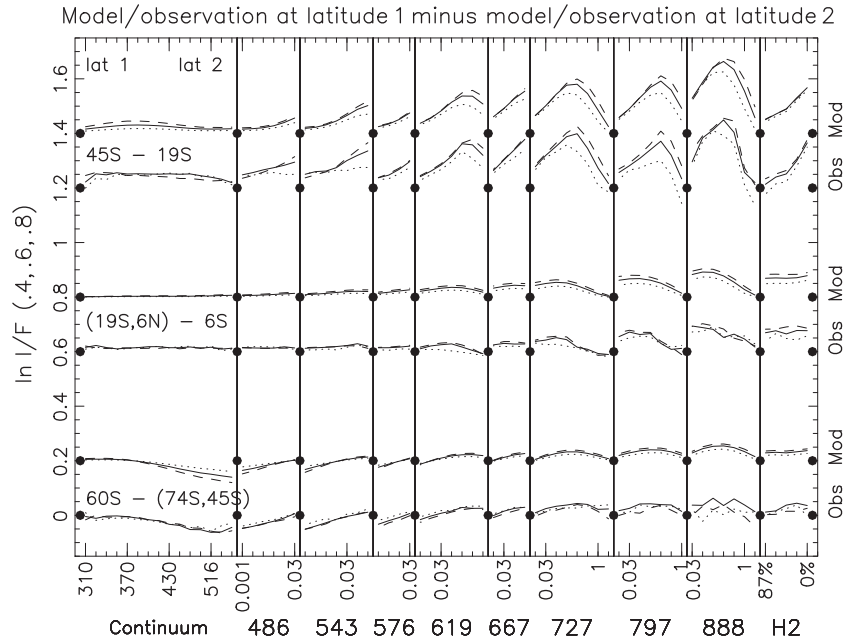


Fig. 12. Observed (Obs) and model (Mod) relative reflectivities between two different latitude regions. The setup is similar to Fig. 11. The first latitude region for the middle case is the average between the 19S and 6N bands, and an analog average applies for the bottom case.

ject previous models that had a constant methane mixing ratio below a certain layer and a constant relative methane humidity above. To explain the data, methane must be significantly variable with latitude around the 2-bar layer, and the vertical extent of that variability must be roughly the 1–3 bar region. Among all possible methane profiles, we chose simple ones that plot as straight lines in the right panel of Fig. 10 with a tangential transition near 1 bar but a kink at 2–3 bars. Theoretical considerations will be needed to refine the profiles into realistic shapes, which may mean no kink.

For the methane profile at 32S we tried two alternate kinds of profiles, those running parallel to the 60S profile, and those with

a common kink near 3.3 bars. Both provided slightly inferior fits, but could not be excluded. Once we adopted our type with a tangential transition near 1 bar, the slope of the profile in the 1.5–2.5 bar region was well constrained by the data.

We now turn to systematic offsets between observations and models. We plot the average of the interior six latitude regions (the southern and northern most ones have inferior limb darkening data), at the top of Fig. 13. The shape of the curves is so different from those in Fig. 11 that no change in model parameters can give significant improvements. For example, the weakest methane absorptions in the 727 and 888 nm methane bands appear about 6% brighter in the model than in the observations. This deviation

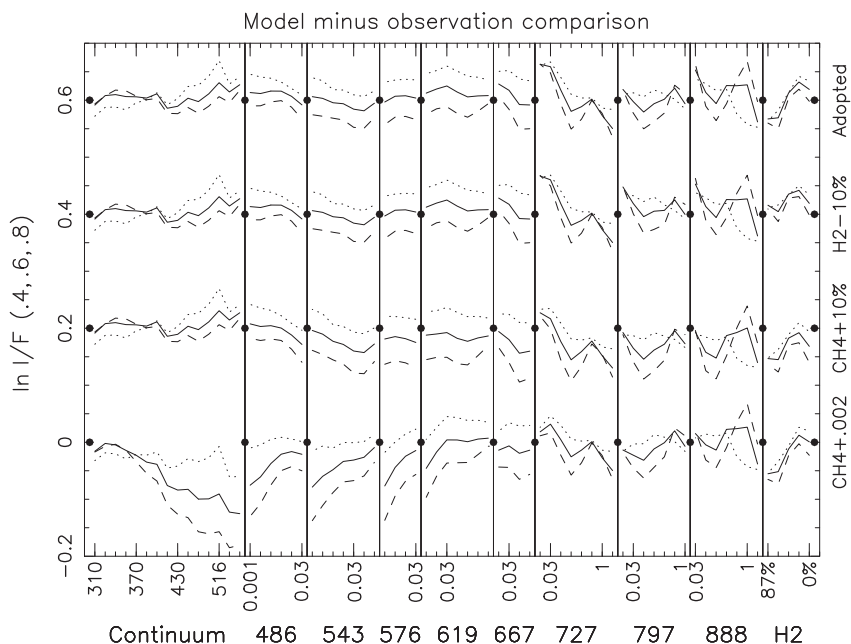


Fig. 13. Comparison between models and observations for the average of the six latitude regions from 60S to 6N for the adopted model (top) and three cases of changed absorption coefficients, a case of all hydrogen absorption coefficients decreased by 10%, a case of all methane absorption coefficients increased by 10%, and a case of all methane absorption coefficients increased by 0.002 km-am⁻¹. The setup is similar to Fig. 11.

could be corrected by increasing the methane absorption coefficients by about 0.002 km-am^{-1} , much smaller than the estimated uncertainty of 0.01 km-am^{-1} (bottom of Fig. 13). A similar though smaller systematic discrepancy occurs for Uranus at the same weak absorptions near 727 and 888 nm (cf. Fig. 22 of K&T2009), suggesting that it is a methane feature. At the weakest absorptions at shorter wavelengths, the 0.002 km-am^{-1} offset causes reflectivity changes of up to 14%, which corresponds to methane abundances along the path of light of up to $0.14/0.002 = 70 \text{ km-am}$, similar to the result in Section 4.2.

Fig. 13 also shows that a 10% change in methane absorption coefficient has a moderate effect on the fit. Furthermore, a 10% decrease in hydrogen absorption coefficients would give a better fit at the hydrogen absorptions (right panel of Fig. 13).

Another significant contribution to the 2.8% residual comes from the systematic difference of the center-to-limb variation between observations and model at visible methane bands (Fig. 13). The model is too bright near the limb (dotted line) and too dark toward the center of the disk (dashed line). The fit would improve by decreasing the methane mixing ratio at deep altitudes, but then the hydrogen absorption region would fit worse, unless methane or hydrogen absorption coefficients are somewhat off in this spectral region. This is possible since weak methane absorptions have not been measured sufficiently well. Laboratory methane abundances go up to one or a few km-am , which are no match to Neptune's 70 km-am .

So far, we determined the four variable parameters of the model for the eight latitudinal regions (dots in Fig. 14). To expand these results to the full latitudinal resolution of our data, we used the relative methane mixing ratio function of Fig. 8 and the method of K&T2009 for the other three parameters, which used the observed reflectivities at each latitude and assumed linearity of model reflectivities as function of parameters within narrow ranges of latitudes.

This “complete” model of Neptune allowed us to calculate model reflectivities for each wavelength and for each location on the disk. For a selection of spectral bands, Fig. 15 shows these synthetic images in the middle and compares them with observed images at the top. The image differences are displayed at bottom. All major observed features on Neptune are well represented in our synthetic images, leaving little room for improvements, although more complicated models could improve slight mismatches. For example, the dark band near -60° latitude was modeled as a latitude band, but it really is a wave where the center latitude varies with longitude (Sromovsky et al., 2001b). Some synthetic images indicate that the whole planet is too bright or too faint, which may be caused by inaccurate absorption coefficients.

7. Comparison with Uranus

7.1. Methane

We compare here our Neptune results primarily with results of K&T2009 about Uranus because both data sets and their analysis were so similar. The most unanticipated result was that Uranus and Neptune have a variable methane profile as function of latitude. For both planets, the methane profile is roughly constant at low latitudes and roughly constant at high southern latitudes, where methane is depleted. For Uranus, the transition is centered on -35° latitude, for Neptune, the best fit is -32° latitude, but consistent with the value for Uranus. The transition region is about 36° wide and similar to the shape of a sine curve.

Hydrogen and methane absorptions near 826 nm wavelength indicate that the ratio of the probed amount between methane and hydrogen is somewhat lower for Uranus than for Neptune, and it varies with latitude by a factor of 2.0 for Uranus but 1.5 for Neptune (cf. Fig. 8). For Uranus, K&T2009 concluded that the methane mixing ratio below the 1.2 bar layer varies between 0.014 at high southern latitudes and 0.032 and northern latitudes. K&T2009 noted that the observations had little sensitivity below the 2 bar level where the haze optical depth became larger than 2. For Neptune, where the haze optical depth stays below 2 to the 12 bar level, we concluded that the high-latitude methane mixing ratio is depressed roughly between 1.2 and 3.3 bars, and that good fits are obtained with sloping profiles (Fig. 10).

A possible physical interpretation is the following. At low latitudes, air rises from deep levels with a constant methane mixing ratio to levels where the methane relative humidity approaches 100%, within a factor of two or so, at which point the mixing ratio decreases rapidly due to the decreasing temperature causing a decreased methane saturation vapor pressure. The dry air is then transported to high latitudes, where it starts to descend. It accumulates methane by some limited rate, which limits the slope of the methane mixing ratio profile to about 20% of the maximum low-latitude slope. Around the 3-bar layer, the methane mixing ratio reaches similar levels as at low latitudes. Such a physical model may provide better clues about the detailed shape of the methane mixing ratio profile than our observations that have a vertical resolution of about half a scale height.

Although the thicker haze on Uranus makes it hard to probe the methane profile below the 2-bar layer, one may speculate whether the methane profiles on Uranus could have similar shapes as those

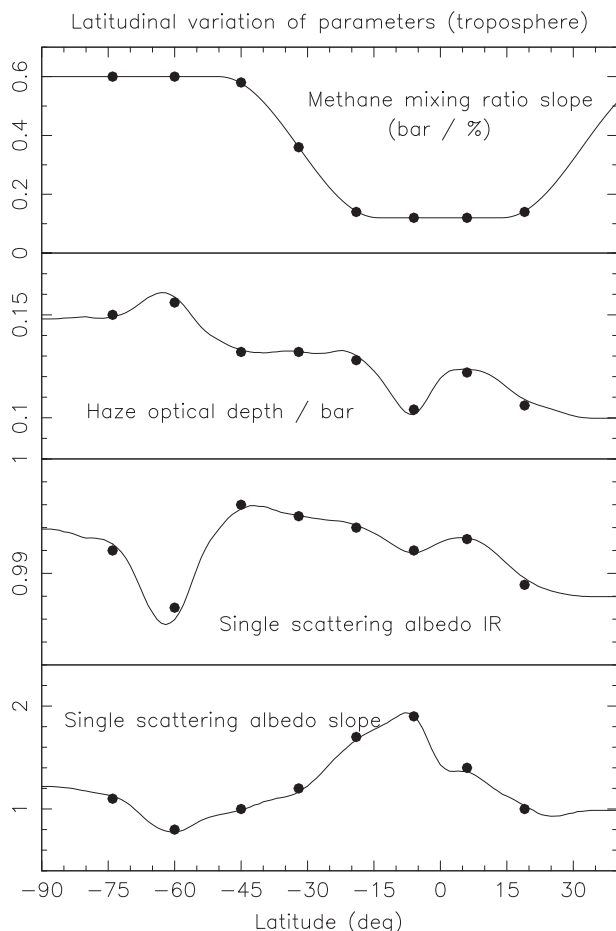


Fig. 14. Latitudinal profiles of the four latitudinal variable parameters of our adopted model for Neptune: the slope of the methane mixing ratio around 2-bar pressure, the tropospheric haze optical depth per bar of pressure, and the single scattering parameters ω_0 and ω_1 (cf. Eq. (2)) for tropospheric aerosols.

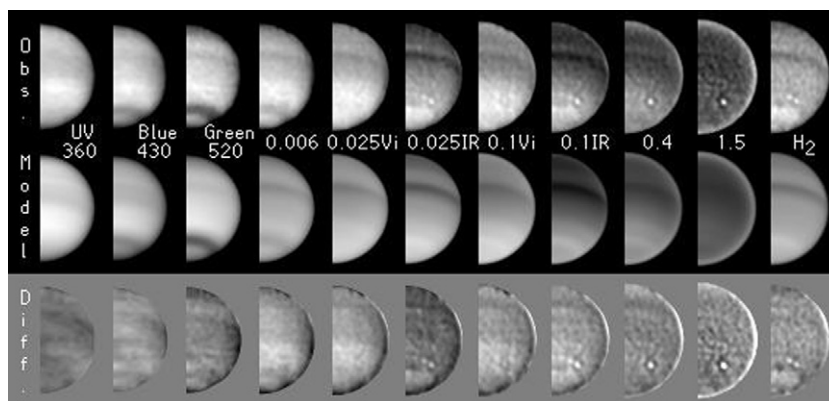


Fig. 15. Observed (top), model (middle), and difference images (bottom) for 11 spectral bands: three continuum bands, several methane absorption strengths, indicated by the methane absorption coefficient in $\text{km}\cdot\text{am}^{-1}$, and the hydrogen absorption band. Images for three methane absorption strengths (0.006, 0.4, and 1.5 $\text{km}\cdot\text{am}^{-1}$) are derived from averaging over all wavelengths, while for two strengths (0.025 and 0.1 $\text{km}\cdot\text{am}^{-1}$), the average is taken separately over wavelengths below 650 nm (Vi) and above 650 nm (IR). Several images are contrast enhanced to bring out features with the top, middle, and bottom images having identical enhancement.

we propose for Neptune. Fig. 10 (left) shows such an attempt that leaves the relative strengths of methane and hydrogen absorptions unchanged. Such a model for high southern latitudes would also need unchanged ratios of haze optical depth to methane abundance down to each level, which means decreased haze optical depths above the 2-bar layer but increased ones further down. At high southern latitudes, profiles of Fig. 10 would require an almost constant haze opacity with altitude, and this value would be similar to the unchanged low-latitude value above the 2 bar layer ($\sim 1.3/\text{bar}$).

The larger latitudinal variation of observed methane to hydrogen absorptions on Uranus (factor of 2) compared to Neptune (factor of 1.5) is reflected in Fig. 10 by different slopes of the methane profile at high latitudes, 1 bar per 0.01 in methane mixing ratio on Uranus versus 0.6 bars per 0.01 on Neptune. This minor difference may reveal insights about physical processes in both atmospheres, which still look very similar with regard to the methane profile.

Our best estimates for the methane mixing ratio at deep layers is 0.032 for Uranus, at least for low latitudes, and 0.04 for Neptune. Both values are accurate to 20–25%, and their relative value is accurate to about 15%. Thus, most likely, Neptune has a slightly higher methane mixing ratio at deep level than Uranus. Our comparison is more reliable than others that were based on observations at specific latitudes or global averages that did not probe sufficiently deep.

Our low-latitude methane mixing ratio for Uranus is well within the range of values determined with Voyager's data (Lindal et al., 1987), also obtained at low latitudes. Our methane mixing ratio for Neptune of 0.04 ± 0.01 is larger than the value of 0.02 ± 0.02 by Lindal (1992). However, Lindal's value was mostly based on latitudes near 60° and altitudes around the 2–3 bar levels. Our methane mixing ratio for the 2–3 bar region at -60° latitude is 0.02–0.03 and thus very consistent with Lindal's determination at latitudes symmetric to the equator.

Our methane mixing ratio of 0.04 ± 0.01 is consistent with the value of 0.03 ± 0.007 by Baines and Smith (1990), which was based on theoretical line strengths for the hydrogen 4-0 quadrupole lines, but inconsistent with the revised range of 0.016–0.027 by Baines et al. (1995), which was based on measured line strengths. The same results occurred for Uranus (cf. K&T2009). Considering that Baines' data were disk averaged, our globally averaged methane mixing ratio in the 1.8–3.8 bar region is about 0.034, closer to Baines' value. Furthermore, Baines used an assumed relative methane humidity of 100% above the 1.5 bar layer, while we used a value of 60% based on weak constraints from our data, which explains another difference of 0.002. Finally, if we use Baines' cloud

structure instead of our haze model, our best-fitting methane mixing ratio decreases slightly. All three systematic effects considered together puts Baines' value only 20% below ours, well within both error bars. As mentioned in Section 6.3, our data in the visible gives better fits for lower methane mixing ratios than the comparison of hydrogen and methane absorptions near 826 nm. Considering Baines' lower methane mixing ratios, our data in the visible may be more reliable, and the 826 nm data may be affected by systematic offsets of absorption coefficients.

7.2. Stratosphere

In the ultraviolet, Neptune's geometric albedo is slightly brighter than Uranus', indicating less absorption from stratospheric aerosols. Stratospheric haze optical depths at unit extinction efficiency (370 nm wavelength) are 0.04 for Neptune versus 0.04–0.07 on Uranus (K&T2009). Stratospheric aerosols on both planets display a similar spectral shape of ultraviolet absorption.

7.3. Tropopause

Uranus and Neptune differ completely near the tropopause. Uranus has a very thin upper tropospheric haze that shows little latitudinal structure, except for a narrow peak centered exactly at the equator (K&T2009). At a few discrete locations, about 2% of the pixels on the disk, cloud features have significant optical depth.

Neptune displays a rich structure of discrete clouds near the tropopause, aligned primarily at a few latitudinal bands, obvious in about 20% of the pixels on the disk. At northern latitudes, the clouds were higher by about one scale height, unless the stratospheric methane mixing ratio was lower at those latitudes. Southern clouds on Uranus are also at lower altitudes than northern ones, but by about two scale heights (K&T2009).

7.4. Troposphere

Starting around 1.2 bars for Uranus and 1.4 bars for Neptune, both planets show an extended tropospheric haze. On both planets, the upper part of the haze is slightly thicker at high southern latitudes than at low latitudes, but Neptune's haze is about 10 times thinner than Uranus'. On Uranus, in particular at low latitudes, the haze thins out below the 2-bar level, while there is no evidence of an altitude variation of Neptune's haze over more than two scale heights.

We found no evidence of a significant variation of optical depth with wavelength on either planet, suggesting that the tropospheric

haze probably consists of aerosols larger than the wavelength. On both planets, the backward scattering part of the phase function is stronger at wavelengths below 500 nm than above 800 nm.

Uranus is an almost bland disk at continuum wavelengths indicating little variation of tropospheric aerosols. On Neptune, contrasts are somewhat larger. At long wavelengths, single scattering albedos may be close to unity at both planets, with a latitudinal variation on Neptune by almost 0.01. In the ultraviolet, the single scattering albedo displays a steep spectral gradient on both planets, with possibly a slightly steeper slope on Neptune, and Neptune's absorption varies by a factor of ~ 2 with latitude.

Voyager occultation data suggested a cloud layer at 1.2 bars for Uranus and 1.9 bars for Neptune (Lindal et al., 1987; Lindal, 1992). Our observations do not show any evidence for such a layer. The opacity enhancement may be too weak to be detectable when looking down on the planet (our data), but still detectable when looking along the planet's limb (Lindal's data).

The spectra of Uranus and Neptune in the 600–1000 nm range are remarkably well correlated, even if just considering the methane windows. Our interpretation is that the absorption is the signature of methane, and aerosol absorption is negligible. On both planets, this signature was considered to be due to strong aerosol absorption (Baines and Hammel, 1994; Sromovsky et al., 2001b), but it seems less likely that the spectral shapes for both planets would be indistinguishable. Furthermore, no investigated laboratory material has such a spectral signature.

Our interpretation of bright aerosols does not work for previous models with a reflective layer at 3–4 bars, which had to make tropospheric aerosols dark to fit the data, because there is insufficient methane above that layer to account for the observed absorption. Models with such a reflective layer can be rejected based on our data at weak methane absorptions. More accurate evaluation of the deep layers of Uranus and especially Neptune will be possible with our data once laboratory measurements with methane abundances similar to those probed on Uranus (up to about 50 km-am) and Neptune (up to about 70 km-am) are available.

K&T2009 proposed a qualitative model for Uranus that has the tropospheric haze produced near the 1.2 bar layer, and the largest haze optical depth where the solar illumination is largest. Aerosols need several years to descend to lower altitudes, where the latitudinal optical depth structure remembers the solar illumination from the past. On Neptune, the solar illumination has been essentially constant for many years, so that the high and low altitudes should have the same latitudinal structure, and the optical depths should be lower at the northern latitudes with low solar illumination. This is just what our results showed. The lower illumination on Neptune compared to Uranus should give lower haze optical depths on Neptune, which we also observed, although by a larger factor than expected.

8. Summary

We analyzed a HST–STIS data cube of Neptune of 0.1 arcsec spatial resolution and 1 nm spectral resolution between 300 and 1000 nm wavelength, calibrated to accuracies of 0.004 arcsec (spatial), 0.05 nm (spectral), and 1% relative and 5% absolute reflectivity. The combination of data about center-to-limb variations over a wide spectral range, methane absorptions with strengths ranging over four orders of magnitude, and hydrogen absorptions, allowed us to test previous results about the vertical and horizontal distribution of methane and aerosols in Neptune's atmosphere. This work on Neptune is similar to the analysis on Uranus from a similar HST–STIS data cube (K&T2009).

While Neptune has been assumed to have a constant methane mixing ratio below the ~ 1.8 bar level, our data indicate that the

methane mixing ratio varies by almost a factor of three with latitude at the 1.8-bar layer, but may be constant at 0.04 ± 0.01 below the ~ 3.3 -bar level (cf. Fig. 10). Most previous measurements of Neptune's methane mixing ratio included data at high latitudes and probed around the 2–3 bar level and thus underestimated the mixing ratio at deep levels. The shape of the latitudinal variation is almost identical to that of Uranus (K&T2009). At high latitudes on both planets, methane-depleted air may be descending fast enough to limit the methane mixing ratio compared to low latitudes, where methane-rich air may be upwelling.

Our ultraviolet data confirmed Neptune's optically thin stratospheric haze (optical depth 0.04 at 370 nm wavelength).

Neptune's obvious features are discrete clouds located near the tropopause. The methane abundance to the cloud top is 0.0026 and 0.0017 km-am for the southern and northern clouds, respectively, in very close agreement with Sromovsky et al. (2001b), indicating remarkable stability. The clouds are bright (reflectivity ~ 0.9) between 540 and 1000 nm wavelength.

A model with a single spatially variable parameter, the filling factor of discrete clouds within the probed area of each pixel on the disk, explained the observed discrete pattern at all wavelengths. The maximum filling factor was $\sim 20\%$, the average 1.7%, the median 0.7%, and 80% of the pixels had values above the 0.2% noise limit. Our model allowed us to “subtract” discrete clouds from the images in order to retrieve features originating from lower altitudes, which have much lower contrasts and thus have been difficult to study.

Low-altitude features derive from tropospheric aerosols in at least four distinct altitude regions, and a simple semi-infinite haze model with a top pressure of 1.4 bars fits our data well. The optical depth varied between 0.10/bar at 25° and 0.16/bar at -60° latitude. These low optical depths allowed probing altitudes below the 10-bar layer.

While the assumption of an optically thick cloud near 3–4 bar pressure (Baines et al., 1995; Sromovsky et al., 2001b) required aerosols to darken significantly longward of 600 nm wavelength, our haze model allows aerosols near unity single scattering albedo at these wavelengths since it attributes the absorption to long methane paths in the deep atmosphere.

A dark, persistent band at visible continuum wavelengths near -60° latitude is caused by a 0.01 decrease of the single scattering albedo. Toward the ultraviolet, the single scattering albedo drops more steeply at low latitudes (to 0.8 at 350 nm) than at mid and high southern latitudes (to 0.9 at 350 nm). Phase functions of tropospheric aerosols have a stronger backscattering peak below 500 nm than above 800 nm wavelength.

Our model for all locations on Neptune sets the filling factor as function of location on the disk and four parameters that are variable with latitude, one for the methane profile and three for tropospheric aerosols, of which one is for the optical depth and two for the single scattering albedos. Synthetic images created from this description are consistent with all major features revealed in our data cube, with a 2.8% rms fit for 1650 key reflectivities.

A qualitative model of production of tropospheric aerosols which then descend to lower altitudes explained the main features observed on Uranus (K&T2009). This model is consistent with some of our key results on Neptune.

Acknowledgments

Support for this work was provided by NASA through Grant No. NNX08AE74G. Support for Program No. HST-GO-09330.01-A was provided by NASA through a grant from the Space Telescope Science Institute, which is operated by the Association of Universities for Research in Astronomy, Incorporated, under NASA Contract NAS5-26555. We thank Patrick Fry for valuable suggestions.

Appendix A

We present a few examples for the definition of our 75 spectral bands.

A.1. Example 1, continuum at 516 nm wavelength

First, we averaged 11 wavelengths between 514.0 and 518.0 nm. They have methane absorption coefficients between 0.0006 and 0.0011 km-am⁻¹ with an average of 0.0008 km-am⁻¹. Then we averaged the 10 wavelengths between 508.0 and 511.6 and the nine between 520.8 and 524.0 nm. They have absorption coefficients between 0.0030 and 0.0105 km-am⁻¹ with an average of 0.0062 km-am⁻¹. The continuum reflectivity at 516 nm was then calculated as 1.245 times the first average minus 0.245 times the second average, based on the non-linearity of reflectivity versus methane absorption coefficients in our models. With perfect linearity, the two weighting factors would need to be 1.15 and 0.15 in order to yield the continuum reflectivity since $1.15 \times 0.0008 - 0.15 \times 0.0062 = 0$. Neptune's geometric albedo peaked at 0.623 in this methane window, with Raman correction at 0.633, with linearity approximation at 0.644, and the inferred continuum albedo was 0.651.

A.2. Example 2, 619 nm methane band at 0.25 km-am⁻¹ methane absorption coefficient

We averaged the 19 wavelengths near 619 nm with methane absorption coefficients between 0.125 and 0.5 km-am⁻¹, which are the 12 wavelengths from 612.8 to 617.2 nm and the seven from 622.0 to 624.4 nm. These 19 data points have an average wavelength of 618.0 nm and an average natural logarithm of methane absorption coefficient of $-1.276 = \ln 0.279$. We used the logarithm here since reflectivity varies close to linearly with the logarithm of methane absorption coefficient in this spectral region. In order to create averages of 619.0 nm and $-1.386 = \ln 0.25$, we weighted the 19 data points by

$$\text{weight} = [1 + 0.0365(\lambda - 619)][1 - 1.36(\ln \kappa - \ln 0.25)]. \quad (5)$$

The first part of the equation increases weights for data points with large wavelengths, which causes a shift of the average wavelength from 618 to 619 nm. The second part of the equation increases weights for data points with small methane absorption coefficients, which causes a shift of the average logarithm from -1.276 to -1.386 . The parameters of 0.0365 and -1.36 in Eq. (5) were found by an iterative method.

A.3. Example 3, hydrogen absorption for 87% relative absorption coefficient

We calculated the average of the 16 wavelengths between 822.4 and 828.4 nm. The hydrogen absorption coefficient for the 16 wavelengths ranged between 70% and 100% of the maximum value (at 826.4 nm), and the average was 87%. Neptune's geometric albedo was 0.155 in this band. We used 80 K temperature for quoting relative coefficients since a model using the absorption coefficient at 80 K yielded the same reflectivity as a model using the absorption coefficient at the actual temperature of each layer.

A.4. Example 4, hydrogen absorption for 67% relative absorption coefficient

We first calculated the average of 16 wavelengths, the 11 wavelengths between 818.0 and 822.0 nm and the five between 828.8 and 830.4 nm. Neptune's geometric albedo was 0.154 in this average. In order to increase Neptune's geometric albedo to the 0.155 value of the previous band, the weighting of the last five data points, where Neptune's geometric albedo was larger, was increased by 3%. This weighting gives an average relative hydrogen absorption coefficient of 67%. We calculated radiative transfer models for each wing of the absorption separately and then computed the weighted average of both model reflectivities, because a single model for the average absorption coefficients yielded slight systematic offsets due to non-linearities.

References

- Baines, K.H., Hammel, H.B., 1994. Clouds, hazes, and the stratospheric methane abundance in Neptune. *Icarus* 109, 20–39.
- Baines, K.H., Smith, W.H., 1990. The atmospheric structure and dynamical properties of Neptune derived from ground-based and IUE spectrophotometry. *Icarus* 85, 65–108.
- Baines, K.H., Mickelson, M.E., Larson, L.E., Ferguson, D.W., 1995. The abundances of methane and ortho/para hydrogen on Uranus and Neptune: Implications of new laboratory 4–0 H₂ quadrupole line parameters. *Icarus* 114, 328–340.
- Burgdorf, M., Orton, G.S., Davis, G.R., Sidher, S.D., Feuchtgruber, H., Griffin, M.J., Swinyard, B.M., 2003. Neptune's far-infrared spectrum from the ISO long-wavelength and short-wavelength spectrometers. *Icarus* 164, 244–253.
- Conrath, B.J., Gautier, D., Lindal, G.F., Samuelson, R.E., Shaffer, W.A., 1991. The helium abundance of Neptune from Voyager measurements. *J. Geophys. Res.* 96, 18907–18919.
- Conrath, B.J., Gautier, D., Owen, T.C., Samuelson, R.E., 1993. Constraints on N₂ in Neptune's atmosphere from Voyager measurements. *Icarus* 101, 168–171.
- Gibbard, S.G., de Pater, I., Roe, H.G., Martin, S., Macintosh, B.A., Max, C.E., 2003. The altitude of Neptune's cloud features from high-spatial-resolution near-infrared spectra. *Icarus* 166, 359–374.
- Hammel, H.B., Lockwood, G.W., 1997. Atmospheric structure in 1994, 1995, and 1996: HST imaging at multiple wavelengths. *Icarus* 129, 466–481.
- Hammel, H.B., Lockwood, G.W., 2007. Long-term atmospheric variability on Uranus and Neptune. *Icarus* 186, 291–301.
- Hammel, H.B., Baines, K.H., Bergstralh, J.T., 1989. Vertical aerosol structure of Neptune: Constraints from center-to-limb profiles. *Icarus* 80, 416–438.
- Heney, L., Greenstein, J., 1941. Diffuse radiation in the galaxy. *Astrophys. J.* 93, 70–83.
- Karkoschka, E., Tomasko, M., 2009. The haze and methane distribution on Uranus from HST-STIS spectroscopy. *Icarus* 202, 287–309.
- Lindal, G.F., 1992. The atmosphere of Neptune – An analysis of radio occultation data acquired with Voyager 2. *J. Geophys. Res.* 97, 967–982.
- Lindal, G.F., Lyons, J.R., Sweetnam, D.N., Eshleman, V.R., Hinson, D.P., Tyler, G.L., 1987. The atmosphere of Uranus: Results of radio occultation measurements with Voyager 2. *J. Geophys. Res.* 92, 14987–15001.
- Moses, J.L., Rages, K., Pollack, J.B., 1995. An analysis of Neptune's stratospheric haze using high-phase-angle Voyager images. *Icarus* 113, 232–266.
- Orton, G.S., Encrenaz, T., Leyrat, C., Puetter, R., Friedson, A.J., 2007. Evidence for methane escape and strong seasonal and dynamical perturbations of Neptune's atmospheric temperatures. *Astron. Astrophys.* 473, L5–L8.
- Pryor, W.R., West, R.A., Simmons, K.E., Delitsky, M., 1992. High-phase-angle observations of Neptune at 2650 and 7500 Å: Haze structure and particle properties. *Icarus* 99, 302–317.
- Smith, B.A., and 64 colleagues, 1989. Voyager 2 at Neptune: Imaging science results. *Science* 246, 1422–1454.
- Sromovsky, L.A., Fry, P.M., 2007. Spatially resolved cloud structure on Uranus: Implications of near-IR adaptive optics imaging. *Icarus* 192, 527–557.
- Sromovsky, L.A., Fry, P.M., Baines, K.H., Dowling, T.E., Baines, K.H., 2001a. Coordinated 1996 HST and IRTF imaging of Neptune and Triton. II. Implications of disk-integrated photometry. *Icarus* 149, 435–458.
- Sromovsky, L.A., Fry, P.M., Dowling, T.E., Baines, K.H., Limaye, S.S., 2001b. Coordinated 1996 HST and IRTF imaging of Neptune and Triton. III. Neptune's atmospheric circulation and cloud structure. *Icarus* 149, 459–488.
- Tomasko, M.G., Doose, L.R., 1984. Polarimetry and photometry of Saturn from Pioneer 11: Observations and constraints on the distribution and properties of cloud and aerosol particles. *Icarus* 58, 1–34.
- Yelle, R.V., Herbert, F., Sandel, B.R., Vervack Jr., R.J., Wentzel, T.M., 1993. The distribution of hydrocarbons in Neptune's upper atmosphere. *Icarus* 104, 38–59.